

Enhancing the performance of catalytic membranes for simultaneous degradation of dissolved organic phosphonates and phosphorous recovery: A fit-for-purpose loose nanofiltration design

Wenjun Wu, Yufei Wang, Kemeng Du, Qiushan Liu, Tong Zhou, Na Wei, Guohan Liu, Jin Guo*

National Engineering Laboratory for Advanced Municipal Wastewater Treatment and Reuse Technology, Beijing University of Technology, Beijing 100124, China

ARTICLE INFO

Keywords:

Loose nanofiltration
Reaction kinetics
Size exclusion
Confinement
Mass transfer

ABSTRACT

In this study, we developed a loose nanofiltration catalytic membrane (LNCM) by incorporating nitrogen-doped carbon nanotubes (NCNT) into graphene oxide (GO) membrane (NCNT@GO-M) to activate peroxydisulfate for efficient phosphonates degradation into phosphate, reducing phosphorus-based pollution and facilitating P recovery. The NCNT@GO-M exhibited superior permeability ($76.7 \text{ L m}^{-2} \text{ h}^{-1} \text{ bar}^{-1}$) due to its expanded pore size (1.60 nm). It integrated nanoconfinement and surface catalysis, improving the availability of surface-bound sulfate radicals for rapid Orth-P generation ($k_{\text{obs}}, 1.93 \text{ s}^{-1}$), with the k_{obs} being 2.4 times higher than that of the NCNT membrane catalytic system and 2626 times higher than the NCNT@GO heterogeneous catalytic system. The NCNT@GO-M also demonstrated excellent antifouling, self-cleaning, and anti-interference ability, effectively retaining humic acid with a molecular weight exceeding 3.6 kDa (~62% removal of dissolved organic carbon), making it suitable for real-water applications. The development of LNCM shows great potential for transforming and recovery of the nutrients in wastewater.

1. Introduction

Phosphorus (P) is a valuable and nonrenewable resource widely used in agriculture [1]. Recently, interest is growing in the use of P-rich wastewater as a valuable alternative P-nutrient resource [2,3]. Phosphonates, an important class of organic phosphorus compounds widely used in industrial and agricultural applications [4], often enter water bodies from runoff and wastewater facilities [5]. As reported, around 7300–8700 tons of phosphonates are discharged annually from agricultural sewage sludge in Europe [6], raising health and environmental concerns due to the remobilization of toxic metals from sediments and harmful byproduct formation during natural hydrolysis (e.g., glyphosate) [7]. Therefore, transforming phosphonate-containing wastewater into inorganic phosphate (Orth-P) can mitigate phosphonate-related risks, while offering a sustainable agricultural P source.

Nanofiltration (NF) membranes have demonstrated significant potential for P-nutrient recovery in wastewater by utilizing size exclusion and/or the Donnan effect to retain them in the feed liquid [8] or separating them from harmful metals [9] and emerging micropollutants [3].

Nevertheless, NF cannot degrade phosphonates into Orth-P. Catalytic membrane (CM), integrating the physical separation and chemical oxidation [10], provides a promising solution for the efficient degradation of phosphonates in wastewater. Currently, loading nanocatalysts onto the membrane platform has been a predominant approach to fabricate CM [11], which enables the generation of reactive oxygen species (ROS) like hydroxyl ($\bullet\text{OH}$) and sulfate radicals ($\text{SO}_4^{\bullet-}$) by activating precursors such as peroxydisulfate (PMS) [12] and hydrogen peroxide (H_2O_2) [13]. Achieving an optimal balance of membrane permeability, exclusion effectiveness, and catalytic efficiency is essential for CM technology. CM with loose structure (e.g., microfiltration/ultrafiltration) cannot prevent the penetration of low and medium molecular weight (MW) organics through the membrane, reducing the availability of ROS for target pollutants and resulting in unsatisfactory degradation efficiency [14]. While CM with dense structure (e.g., NF) always sacrifices the permeability and increases energy costs [15]. Therefore, loose NF membranes with catalytic function (LNCM) offers a viable solution, combining the catalysis and higher permeability than traditional NF [16].

* Corresponding author.

E-mail address: guojin@bjut.edu.cn (J. Guo).

<https://doi.org/10.1016/j.apcatb.2024.124118>

Received 18 March 2024; Received in revised form 16 April 2024; Accepted 23 April 2024

Available online 24 April 2024

0926-3373/© 2024 Elsevier B.V. All rights reserved.

Two-dimensional (2D) laminar membranes, particularly graphene oxide (GO) membranes, are promising for LNCM construction, often enhanced by anchoring metal-based nanocatalysts to improve permeability and catalytic activity [17,18]. Cobalt single atom (Co_1) demonstrated exceptional catalytic effectiveness for 1,4-dioxane [19], while its intercalation slightly improved permeability with limited effects on the expansion of membrane pore size. Besides, metal-based catalysts could pose an inherent risk of metal leakage [20]. Carbon nanotubes (CNTs) and derivatives, as intercalating nanomaterials, hold promise in addressing the trade-off between permeability and selectivity in GO membranes, and reducing environmental risks from metal nanocatalysts [21,22]. Nevertheless, the applications of GO-intercalated membranes have focused on the separation of dyes/salts in industrial wastewater (Table S1), with limited attention on catalytic performance [23,24].

In catalysis processes, radicals generated can either be distributed in the bulk solution as free radicals or localized at the catalyst surface/

interface, known as surface-bound radicals [25]. The ultrashort lifetime of free radicals hinders their transport from the catalyst surface to bulk solution for pollutants degradation [26]. Therefore, the enhancement of free radical's yield cannot significantly improve pollutant degradation efficiency. Instead, designing surface-bound radicals dominated catalytic reactions, the oxidation of pollutants primarily occurs on the catalyst surface/interface, can significantly improve the availability of radicals [27]. Among the reported surface-bound radicals, surface- $\text{SO}_4^{\cdot-}$ stands out in PMS-based advanced oxidation processes (AOPs) due to its stronger oxidation ability ($E_0 = 2.5\text{--}3.1\text{ V}$), higher selectivity, and remarkably long lifetime ($82.58\text{ }\mu\text{s}$) [28]. Zhang et al. [29] proposed that surface-bound radicals tended to generate on the surface of CNTs due to their π -network of graphene sheets in contrast to metal oxides. Wang et al.'s group [30–32] also observed a similar phenomenon, that surface-bound radicals can be readily generated on the surface of carbon materials. Particularly, nitrogen-doped carbon materials, where

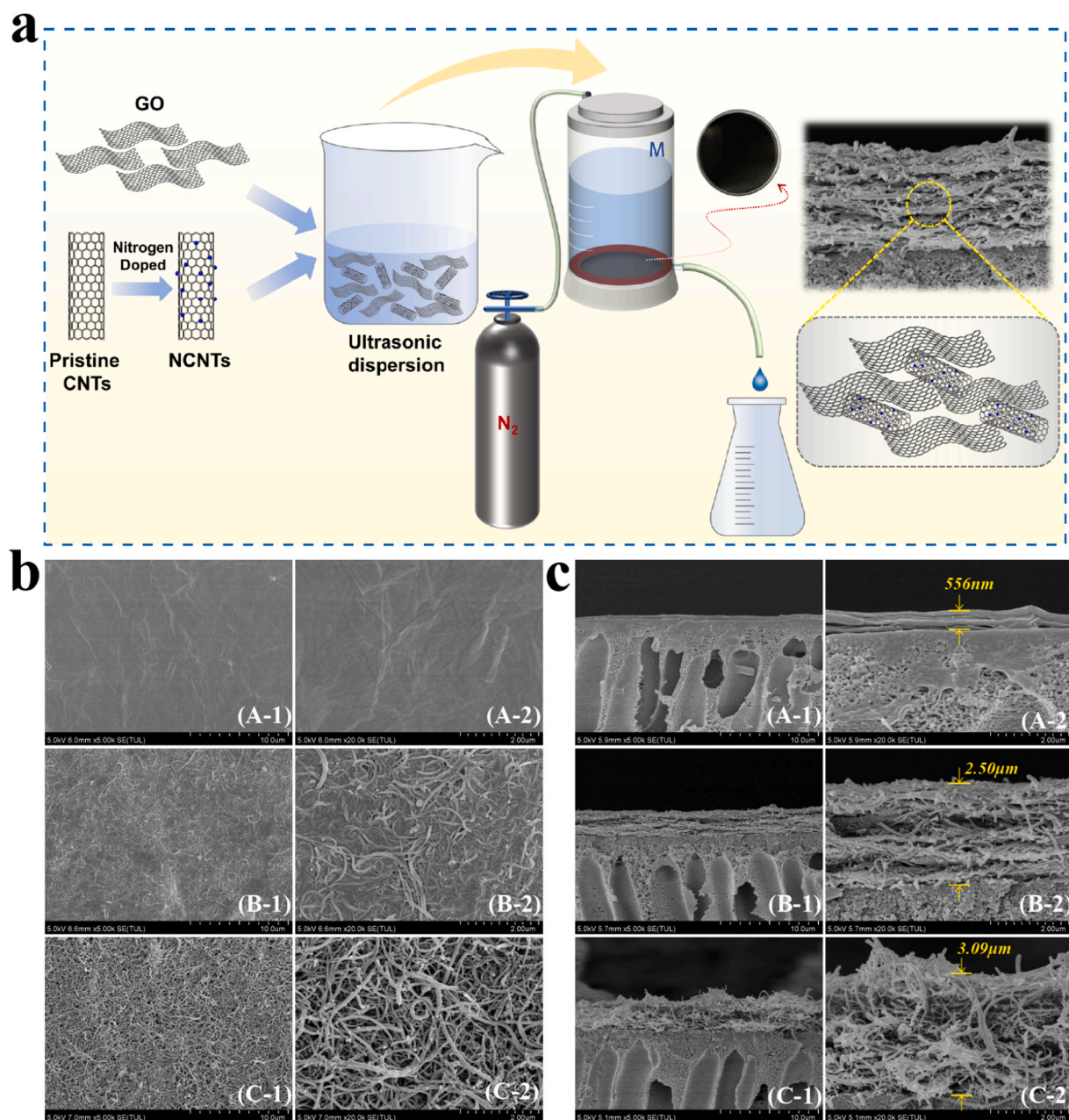


Fig. 1. (a) Schematic illustration of the preparation process. SEM images of (b) membrane surface and (c) the cross-section: (A) GO-M, (B) 60NCNT@GO-M, (C) NCNT-M (1: low-resolution, $\times 5.0\text{ K}$; 2: high-resolution, $\times 20.0\text{ K}$).

nitrogen serving as Lewis base sites enhances the adsorption and activation for oxidants (acting as Lewis acid sites), create a conducive environment for the generation of surface-bound radicals [33]. Inspired by this, anchoring NCNT into GO membrane might have a potential to produce surface-bound radicals.

In this study, we fabricated a fit-for-purpose LNCM by inserting NCNT into the GO membrane (NCNT@GO-M). The aim is to construct a NCNT@GO/PMS catalytic system which generates surface- $\text{SO}_4^{\bullet-}$, promoting phosphonates degradation within nanoconfined GO-laminates. Taken refractory ethylenediamine tetra(methylene phosphonic acid) (EDTMP) as the target pollutant, we investigated the permeability, catalytic performance and exclusion effectiveness of the NCNT@GO-M. Besides, we systematically investigated the contribution of the surface- $\text{SO}_4^{\bullet-}$ for EDTMP degradation by using electron paramagnetic resonance (EPR), classical quenching tests and electrochemical analysis, with fluorescence microscopy providing visualization into its spatial distributions. The study aims to: (i) design a LMNC for effective degradation of phosphonate to Orth-P; (ii) investigate the mechanism of nanoconfined NCNT@GO-M/PMS to enhance reaction kinetics of phosphonates; (iii) evaluate potential applications of the NCNT@GO-M in water treatment, including self-cleaning, antifouling properties, universality and stability. This work underscores a novel approach for P-nutrient recovery from wastewater through a customized membrane design.

2. Materials and methods

2.1. Preparation of NCNT@GO membrane and characterization

Details regarding the chemicals were provided in the [Supporting Information](#) (Text S1). The NCNT@GO membrane (NCNT@GO-M) consists of a commercial PES (100 kDa) support and a catalytic layer of GO intercalated with NCNT, with the preparation process illustrated in [Fig. 1a](#). The NCNTs were first prepared according to our previous work [34]. The dispersions of NCNT and GO were prepared before the fabrication of NCNT@GO-M. Subsequently, the dispersions of NCNT (0.25 mg mL^{-1}) and GO (0.25 mg mL^{-1}) were mixed, and a series of composite membranes with different NCNT intercalation ratios (0%, 30%, 45%, 60%, and 75%) were obtained by pressure-assisted filtration method. For comparison, two control samples were prepared: 1) a pure NCNT membrane (NCNT-M), representing a “non-confined” system due to its broader catalytic reaction space unrestricted by GO nanosheets compared to NCNT@GO-M; 2) NCNT@GO powder (NCNT@GO-P), which serves as the “unconfined” counterpart to NCNT@GO-M, representing a traditional “unconfined” system with catalyst and reactants in the bulk phase. The detailed fabrication process was described in Text S2, and membrane characterization was available in Text S3.

2.2. Membrane permeability and catalytic performance evaluation

Membrane filtration and catalytic tests were conducted in a dead-end ultrafiltration cup (Amicon 8200, Millipore, USA) with an effective membrane area of 28.7 cm^2 under room temperature of $23 \pm 2^\circ \text{C}$ ([Fig. S1](#)). The [Supporting Information](#) (Text S5) provided a detailed introduction to the determination of membrane permeability.

The catalytic performance of the NCNT/GO-M was optimized by adjusting NCNT/GO ratios, PMS concentration and NCNT dosage. In a typical catalytic experiment, the feed solution containing 0.4 mM PMS and $50 \mu\text{M}$ EDTMP was pumped through the membrane under a trans-membrane pressure (TMP) of 0.2 bar , without pH adjustment. Permeates samples were collected at set intervals, with methanol (1 mL) added to stop the reaction. The catalytic performance of the NCNT@GO-M was evaluated by calculating first-order rate constant (k_{obs}) for Orth-P generation, with details in Text S6. In comparison, the k_{obs} in NCNT-M and NCNT@GO-P catalytic system, representing a non-confined membrane filtration and traditional unconfined systems respectively, was also determined. For the NCNT@GO-P heterogeneous catalytic system,

NCNT@GO-P (40 mg L^{-1}) and 0.4 mM L^{-1} of PMS were added into a 100 mL beaker, under a stirring rate of 250 rpm at room temperature. For the NCNT-M catalytic system, the experimental parameters were kept the same as the NCNT@GO-M, except for the addition of GO nanosheets. The obtained water samples were collected for water quality analysis. The detailed analysis methods can be found in Text S7.

To verify the main ROS, radicals quenching experiments, EPR technique, electrochemical measurements, 3D-fluorescence spectroscopy and fluorescence microscopy observation were conducted. Additionally, quenching experiments were performed in both NCNT@GO-M and NCNT@GO-P catalytic systems to compare the relative contribution of each ROS based on the k_{obs} (Text S8).

Five cycle filtration experiments were conducted to assess the stability of the NCNT@GO-M. To demonstrate the universality of the NCNT@GO-M, degradation experiments on several common phosphonates ($50 \mu\text{M}$), such as 1-hydroxyethane 1,1-diphosphonic acid (HEDP), nitrilotris(methylene phosphonic acid) (NTMP), and hexamethylenediamine tetra(methylene phosphonic acid) (HDTMP) were performed. All tests were conducted at least for three times.

2.3. Anti-interference ability evaluation of NCNT@GO membrane

To evaluate the anti-interference ability of the NCNT@GO-M, 5 mg-C L^{-1} HA was added to a mixture of EDTMP ($50 \mu\text{M}$) and PMS (0.4 mM), and measuring the k_{obs} in the presence of HA. This was compared with the NCNT-M and NCNT@GO-P systems to evaluate the system's anti-interference robustness, represented by the reduction in k_{obs} . For insight into the exclusion for HA by NCNT@GO-M, three-dimensional EEM and high-performance size exclusion chromatography (HPSEC-UV) were employed to determine the change of fluorescence components and MW distribution (MWD) (Text S7). Additionally, the anti-interference ability of the NCNT@GO-M for EDTMP degradation was tested under varied water matrix conditions, including different pH levels, inorganic ions, and actual water samples (tap water, laboratory-scale Anaerobic-Anoxic-Oxic Membrane Biological Reactor ($\text{A}^2\text{O-MBR}$) effluent, secondary effluent of a WWTP (Beijing, China), surface water from a water treatment influent (Shanghai, China), and drinking water from a drinking water treatment plant effluent (Shanghai, China)).

2.4. Membrane antifouling and self-cleaning assessment

To assess the antifouling and self-cleaning properties of NCNT@GO-M, dynamic filtration experiments were conducted using a single-HA solution (5 mg-C L^{-1}) with and without the addition of 0.4 mM PMS. The initial water flux of the NCNT@GO-M was measured and denoted as J_0 . Subsequently, the HA solution was introduced to the feed solution for a 90-minute dynamic filtration under a TMP of 0.2 bar . The permeate flux (J) was monitored to obtain the normalized flux (J/J_0). Analogous fouling experiments were also conducted using WWTPs effluent and surface water to validate practical applications. During the catalysis and filtration processes by the NCNT@GO-M, EEM, HPSEC-UV and total organic carbon (TOC) analyzer were used to characterize the variation of fluorescent substances, MWD and dissolved organic carbon (DOC), respectively.

3. Results and discussion

3.1. Characterization of NCNT@GO membrane

The morphology of the membranes was characterized using scanning electron microscope (SEM). [Fig. 1b\(A\)](#) showed a smooth and thin film morphology of the GO-M. Following NCNT intercalation, the membrane surface became rougher, as seen in [Fig. 1b\(B\)](#) and [Fig. S2a](#). NCNT and GO stacked tightly and evenly on the PES support without obvious defects or aggregation, indicating well-dispersed GO nanosheets and NCNT. Notably, the magnified SEM image ([Fig. 1b\(B-2\)](#)) revealed a thin

mist-like coating on the membrane top, with the tubular structure of NCNT (Fig. 1b(C)) embedded in adjacent nanosheets, indicating successful intercalation of NCNT into GO. The thickness of the GO-M was ~ 556 nm (Fig. 1c(A)). As the NCNT intercalation ratio increased from 30% to 75%, the thickness of the NCNT@GO-M increased from ~ 798 nm to ~ 2.93 μm (Fig. 1c(B) and Fig. S2b). This interlayer expansion of GO-laminates was attributed to NCNT intercalation, which created more continuous 3D-nanochannels. This result was further confirmed by transmission electron microscopic (TEM) image (Fig. S3), which showed that RGO nanosheets, possessing many wrinkles, were closely integrated with NCNT, which present an intact tubular cavity structure, together forming a robust and stable network. Additionally, the introduction of NCNT significantly enhanced the hydrophilicity of the GO-M, with the water contact angle decreasing from $\sim 42^\circ$ to 12.5° (Fig. S4). Fig. S5a demonstrated NCNT@GO-M has greater mechanical strength than GO-M, maintaining structural integrity after ultrasonication (60 kHz, 100 W) for 10 min. Surprisingly, NCNT@GO-M can be peeled off from the PES support easily (Fig. S5b).

FTIR, Raman, XRD and XPS patterns of GO-M, NCNT-M and NCNT@GO-M were shown in Fig. S6. In the FTIR patterns (Fig. S6a), the N-H peak was observed in both NCNT-M and NCNT@GO-M, indicating successful intercalation of NCNT. From the Raman spectra (Fig. S6b), typical D and G bands were located at 1350 and 1596 cm^{-1} , respectively. Following NCNT intercalation, NCNT@GO-M showed a lower Raman D/G peak height ratio ($I_D/I_G = 0.927$) than GO-M ($I_D/I_G =$

0.966), indicating the enhanced graphitization degree of NCNT@GO-M after NCNT intercalation. The high graphitization degree of NCNT ($I_D/I_G = 0.618$) is favorable for electron transfer during catalysis [24]. The XRD spectra (Fig. S6c) showed a typical peak at $2\theta = 10.85^\circ$ appeared on the GO-M [35], with a dominant peak at about 25.95° (corresponding to crystal plane (002) of CNT) in NCNT-M [36]. For NCNT@GO-M, the intensity of GO's characteristic diffraction peak was slightly weakened, suggesting preserved microstructures of GO-M. The XPS spectra (Fig. S6d) showed that the N level increased from 0.62 atom% (GO) to 1.31 atom% (NCNT@GO) due to NCNT intercalation. The high-resolution XPS N 1s spectrum (Fig. S7) revealed graphitic N in both NCNT and NCNT@GO samples, which confirmed the successful N-doping into CNT and the preservation of graphitic N species after intercalation. These results indicated that NCNT intercalation modulated the structure and surface properties of NCNT@GO-M.

3.2. Catalytic performance of NCNT@GO membrane and structure optimizing

EDTMP was chosen as a typical phosphonate to evaluate the catalytic performance of the NCNT@GO-M/PMS system. And this was contrasted against PMS oxidation and NCNT@GO-M filtration in removing or degrading EDTMP to Orth-P. Fig. 2a demonstrated that the NCNT@GO-M/PMS system completely removed EDTMP within one minute and maintained this effectiveness throughout the experiment. During

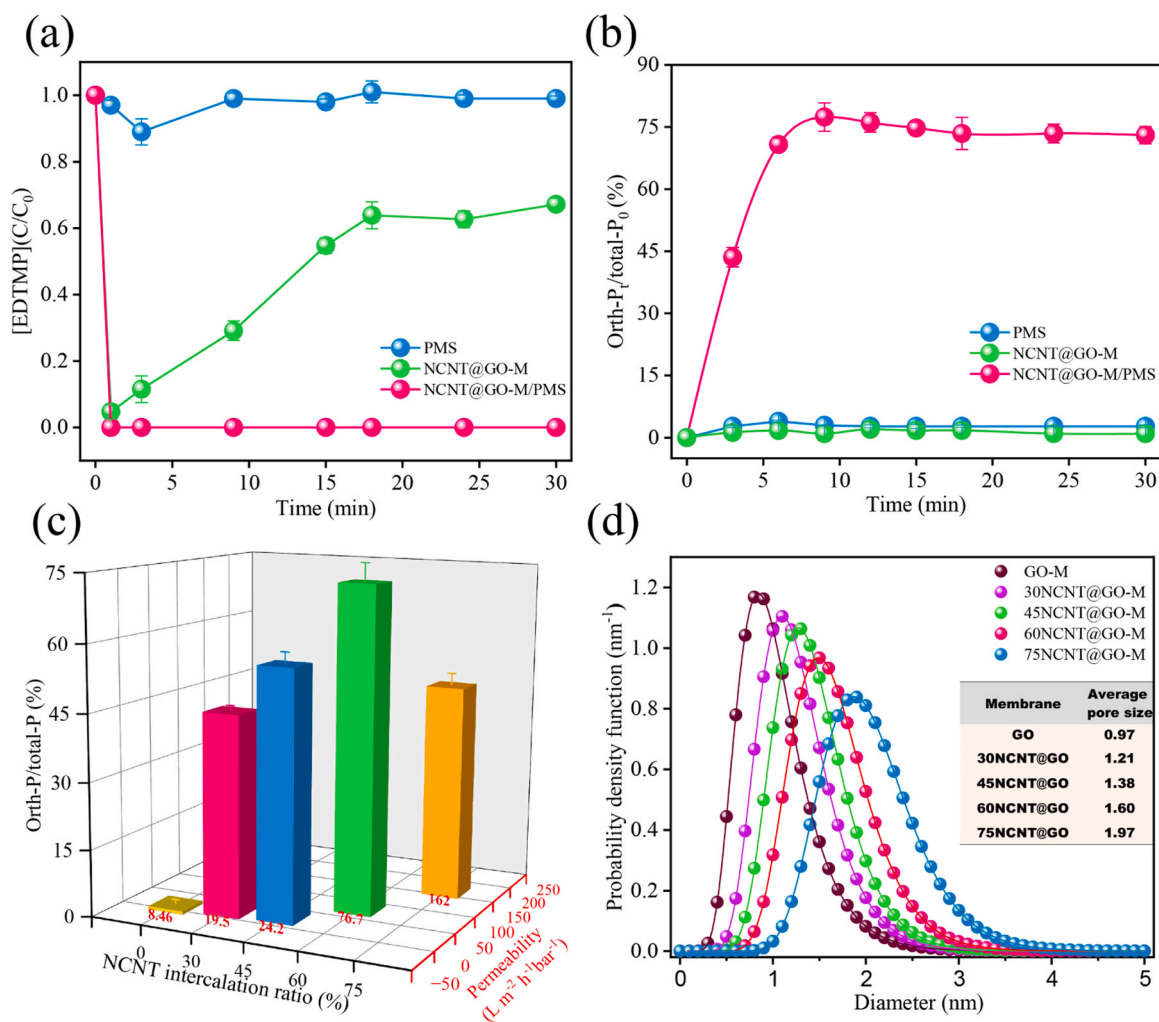


Fig. 2. (a) EDTMP degradation and (b) Orth-P generation in different systems. (c) Orth-P production rate and permeability with different NCNT intercalation ratios. (d) The pore size distribution and average pore size (the inset) of NCNT@GO-M. Conditions: $[\text{EDTMP}]_0 = 50\text{ }\mu\text{M}$, $[\text{PMS}]_0 = 0.4\text{ mM}$, without adjusting pH.

NCNT@GO-M filtration, a 95% removal rate of EDTMP was achieved within one minute, but dropped quickly to 32.8% because of adsorption saturation. The effects of PMS oxidation on EDTMP removal was examined in a traditional homogeneous catalytic system. The results showed PMS oxidation barely removed EDTMP. This could be attributed to the structural stability of EDTMP (Table S2), featuring four phosphonic acid groups and covalent C-P bonds. Correspondingly, the Orth-P production was illustrated in Fig. 2b. In the NCNT@GO-M/PMS system, approximately 75% of total phosphorus (TP) in EDTMP was transformed to Orth-P, whereas the NCNT@GO-M filtration and PMS oxidation failed to degrade EDTMP to Orth-P. In combination, the degradation and transformation of EDTMP could be realized in the NCNT@GO-M/PMS system, where ROS with higher oxidation ability than PMS (standard redox potential of 1.75–1.82 V_{NHE}) could be generated.

NCNT@GO-M's structure was further optimized to balance catalytic activity and permeability by adjusting the NCNT intercalation ratio. Fig. 2c illustrated that Orth-P production rate increased from 0.7% to 73.0% with NCNT intercalation ratio increasing from 0% to 60%, then fell to 43.0% as it increased to 75%. This could be due to the structure disruption of the 75NCNT@GO-M. Specifically, compared with the 60NCNT@GO-M, the 75NCNT@GO-M had a lower proportion of GO. With this lower proportion, GO was unable to completely encapsulate NCNT, leaving some NCNT exposed on the GO nanosheet's outermost layer. As depicted in the structural morphology of the membrane (Fig. S2a(C-2)), the dense layered structure of GO in 75NCNT@GO-M was disrupted. The disruption caused by overloading NCNT could lead to uneven dispersion of NCNT, thereby affecting catalytic efficiency.

By adjusting NCNT intercalation ratio, the permeability of NCNT@GO-M changed as the size of interlayer nanochannels in the GO

membrane (i.e., pore size) was modified [22]. As shown in Fig. 2c, as the NCNT ratio increasing from 0% to 75%, the corresponding permeability of NCNT@GO-M increased from 8.46 to 162 L m⁻² h⁻¹ bar⁻¹. The average pore size of NCNT@GO-M increased from 0.97 to 1.97 nm (Fig. 2d). Despite 75NCNT@GO-M exhibited highest permeability, its disrupted structure might result in undesirable catalytic efficiency. Given a balance between permeability and catalytic activity, 60NCNT@GO-M was identified as the optimal configuration. Notably, the permeability of 60NCNT@GO-M reached 76.7 L m⁻² h⁻¹ bar⁻¹, which was about 1.5–7.6 times higher than the values of other reported analogous CNT intercalated GO membranes (Table S1). The enhancement in permeability could be attributed to the relatively looser membrane pore (1.60 nm), which were larger than the pore sizes (0.85–1.51 nm) observed in other membranes.

Subsequently, the effects of NCNT dosage (surface density) and PMS concentration on catalytic performance of 60NCNT@GO-M (referred to as NCNT@GO-M for convenience) were investigated. The optimal NCNT dosage was 0.2 mg cm⁻² (Fig. S8a), with the optimal PMS concentration established at 0.4 mM (Fig. S8b). Compared with our previous study [34], where only about 60% of Orth-P was transformed with NCNT dosage of 0.5 mg cm⁻² and PMS concentration of 0.5 mM, this NCNT@GO-M/PMS system achieved a higher Orth-P yield (~75%) while reducing the consumption of catalyst (NCNT) and oxidant (PMS).

3.3. Reaction kinetics of EDTMP in the NCNT@GO-M catalytic system

The reaction kinetic of EDTMP in the NCNT@GO-M catalytic system was evaluated using the first-order rate constants (k_{obs}) for Orth-P generation. The k_{obs} was deduced based on different retention times

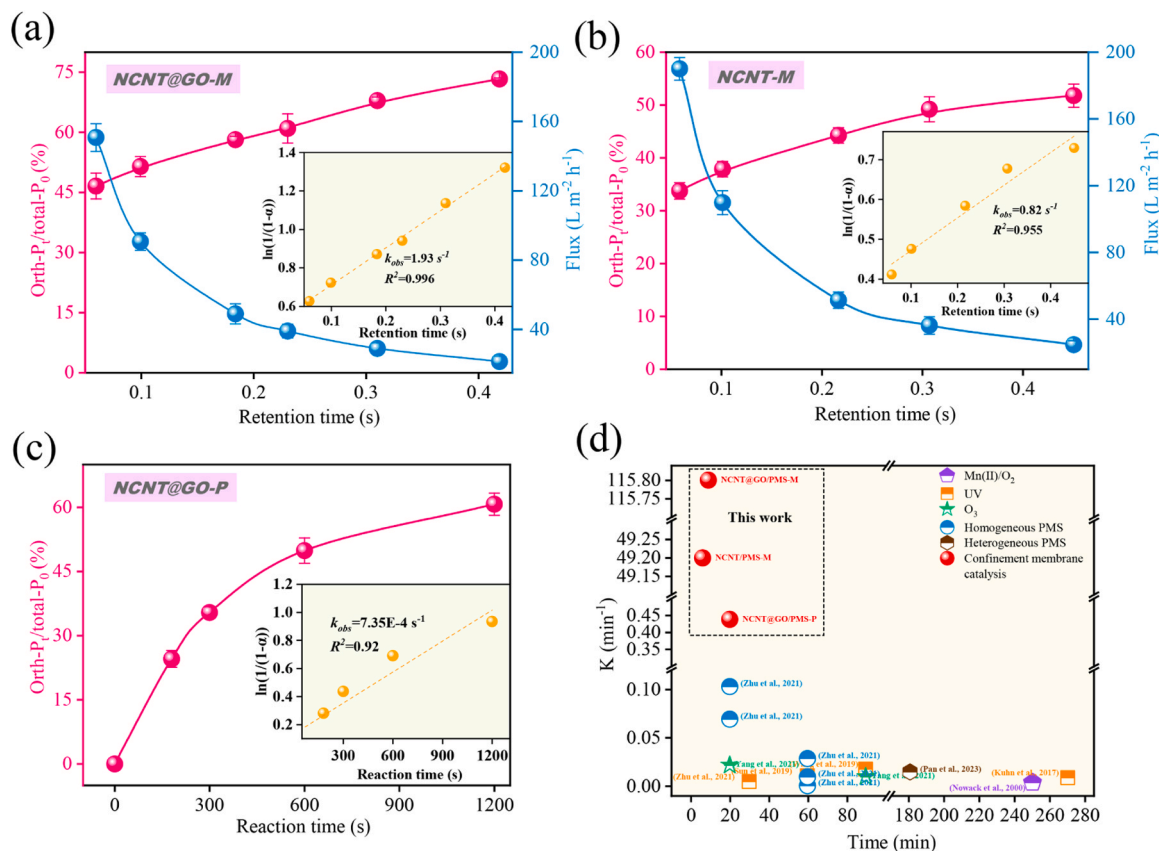


Fig. 3. Retention time versus Orth-P production rate and flux in different catalytic systems: (a) NCNT@GO-M, (b) NCNT-M, and (c) NCNT@GO-P. The inset figures show the kinetics determined by linear regression analysis. After 30-minutes reaction, permeate samples were obtained to measure the Orth-P concentration for kinetic analysis. (d) Comparison of the first-order rate constants for Orth-P generation by different catalytic systems. Conditions: [TMP] = 0.1–2.0 bar for (a–b), [PMS]₀ = 0.4 mM, [EDTMP]₀ = 50 μM, without adjusting PH.

related with membrane flux by changing TMP (Text S6). Control experiments were conducted in the NCNT-M and NCNT@GO-P catalytic system. Fig. 3a illustrated the profile of Orth-P production rate as a function of retention time. An increase in retention time signifies a decrease in membrane flux, conceptually equivalent to extending the reaction time in a powder heterogeneous catalytic system. About 75% Orth-P was formed in the NCNT@GO-M catalytic system, with a retention time of approximately 0.45 s (equivalent to a permeation flux of $21.5 \text{ L m}^{-2} \text{ h}^{-1}$), and the k_{obs} reached 1.93 s^{-1} (inset in Fig. 3a). In comparison, k_{obs} for NCNT-M and NCNT@GO-P catalytic system was 0.82 s^{-1} (inset in Figs. 3b) and $7.35 \times 10^{-4} \text{ s}^{-1}$ (inset in Fig. 3c), respectively. Remarkably, k_{obs} values for NCNT@GO-M were about 2.4 and 2626 times greater than those of NCNT-M and NCNT@GO-P, and 3–5 orders of magnitude above previously reported values (Fig. 3d, Table S2). These results underscored the crucial role of the nanoconfined structure of NCNT@GO-M in enhancing reaction kinetics.

As reported, the presence of nature organic matters (NOM) may occupy active sites on catalysts or scavenge the ROS [13], thereby impairing the degradation efficiency of target pollutants. NCNT@GO-M was composed of a GO separation layer and the catalyst-NCNT embedded between adjacent GO nanosheets. To investigate the effectiveness of NCNT@GO-M in mitigating NOM interference, 5 mg L^{-1} HA, a representative NOM, was introduced into a reaction solution containing EDTMP and PMS. Reaction kinetics for EDTMP were further examined in the NCNT@GO-M catalytic system, and the results were compared with NCNT-M and NCNT@GO-P catalytic systems. In the presence of HA, a significant inhibition was observed in NCNT@GO-P catalytic system, with k_{obs} decreasing to $3.38 \times 10^{-5} \text{ s}^{-1}$ (Fig. S9a). Similarly, k_{obs} demonstrated an obvious decline in the NCNT-M catalytic system (0.47 s^{-1} , Fig. S9b). Conversely, HA's interference was negligible in the NCNT@GO-M catalytic system, with only slight decrease in k_{obs} from 1.93 s^{-1} to 1.71 s^{-1} (Fig. S9c). Fig. 4a revealed that, after being interfered by HA, NCNT@GO-M showed 88.6% anti-interference robustness (11.4% reduction in k_{obs}), whereas NCNT-M and NCNT@GO-P exhibited merely 57.3% (42.7% reduction in k_{obs}) and 5% (95% reduction in k_{obs}) anti-interference robustness, respectively. The excellent anti-interference ability of NCNT@GO-M was primarily attributed to the size exclusion effect. The exclusion effectiveness was further confirmed by the changes in MWD and DOC of HA observed before and after NCNT@GO-M filtration (Fig. 4b). The influent HA had a MW of about 4.5 kDa, consistent with previous reports [37]. After NCNT@GO-M filtration, the SEC curve exhibited a significant decrease in peak intensity, resulting in 63% of DOC removal. The majority of HA

was excluded by NCNT@GO-M as it exceeding the pores size (3.6 kDa, as calculated by the PEG retention method in Text S4). Conversely, EDTMP ($\sim 0.848 \text{ nm}$) and PMS precursor molecules ($\sim 0.514 \text{ nm}$), with respect to their van der Waals diameters (as detailed in Text S9), are significantly smaller than pore size (1.60 nm), enabling easy access to catalytic sites within the membrane pores. Since the NCNT were shielded from the majority of HA, NCNT@GO-M was able to selectively target EDTMP degradation. Furthermore, after NCNT@GO-M catalysis, there was a further reduction in the peak intensity of the SEC curve and a shift toward lower MW, with the DOC removal rate decreasing to below 20%. This suggested that NCNT@GO-M catalysis promoted the decomposition of HA into smaller molecules or fragments ($\sim 2.8 \text{ kDa}$), which could pass through the membrane pores, leading to higher DOC levels in the effluent. In conclusion, NCNT@GO-M can effectively exclude the majority of high-MW HA, thereby mitigating its negative impact on EDTMP degradation to Orth-P.

3.4. Verifying surface-bound radicals

3.4.1. Probing radicals

$\bullet\text{OH}$ and $\text{SO}_4^{\bullet-}$ are common reactive species in carbon-based/PMS catalytic system. EPR tests (Text S10) were conducted to detect both of these radicals using 5,5-dimethyl-1-pyrroline-N-oxide (DMPO) as a spin trapping reagent. Fig. 5a illustrated the presence of characteristic signal peaks corresponding to DMPO-OH (1:2:2:1) and DMPO- $\text{SO}_4^{\bullet-}$ (1:1:1:1:1:1) adduct signals, suggesting the potential generation of $\bullet\text{OH}$ and $\text{SO}_4^{\bullet-}$.

Tert-butyl alcohol (TBA) and methanol (MeOH) were used as scavengers for radicals. MeOH can effectively quench both $\bullet\text{OH}$ and $\text{SO}_4^{\bullet-}$ ($k_{\text{OH,MeOH}} = 9.7 \times 10^8 \text{ M}^{-1} \text{ s}^{-1}$; $k_{\text{SO}_4^{\bullet-},\text{MeOH}} = 3.2 \times 10^6 \text{ M}^{-1} \text{ s}^{-1}$) [38]. TBA can scavenges $\bullet\text{OH}$ but is less effective for $\text{SO}_4^{\bullet-}$ ($k_{\text{OH,TBA}} = 7.6 \times 10^8 \text{ M}^{-1} \text{ s}^{-1}$; $k_{\text{SO}_4^{\bullet-},\text{TBA}} = (4-9.1) \times 10^5 \text{ M}^{-1} \text{ s}^{-1}$) [38,39]. Fig. 5b showed that the Orth-P generation was only slightly inhibited with high concentrations (1 M) of TBA or MeOH, suggesting that free $\bullet\text{OH}$ and $\text{SO}_4^{\bullet-}$ were not the main ROS responsible for EDTMP degradation.

3.4.2. Probing singlet oxygen ($^1\text{O}_2$)

The main oxidation role of $^1\text{O}_2$ has also been reported in N-doped carbon materials/PMS systems [40]. To investigate the presence of $^1\text{O}_2$, EPR tests were performed using 2,2,6,6-tetra-methyl-4-piperidone (TEMP) as a spin trapping reagent. The typical triplet adducts signal characteristic peaks (height ratio 1:1:1) of 2,2,6,6-tetramethylpiperidine-N-oxide (TEMPO) were observed in Fig. 5c. However, this signal

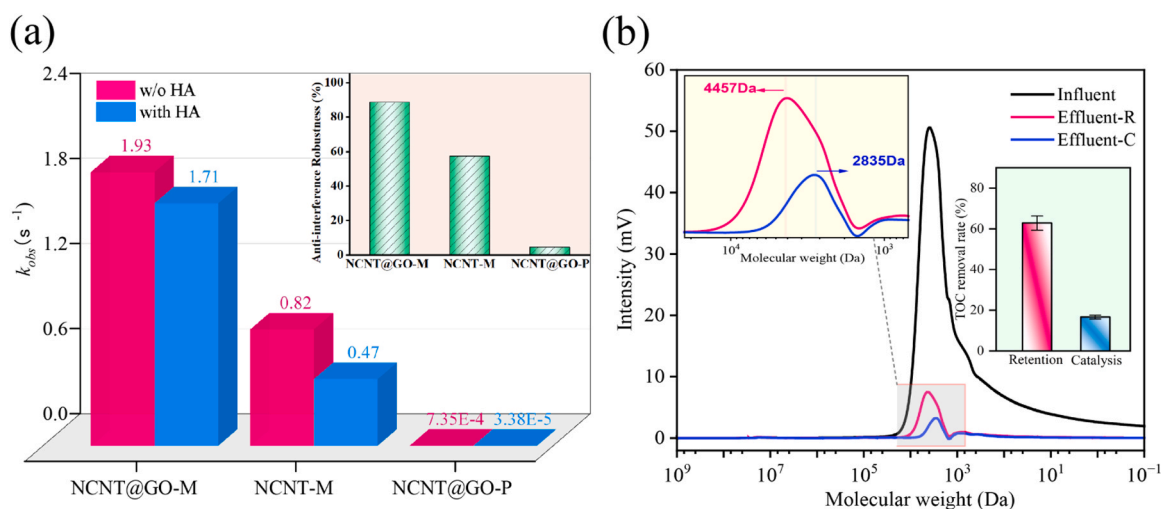


Fig. 4. The effects of HA interference on k_{obs} and the inset figures show the anti-interference robustness in different catalytic systems (a). The change of SEC profiles and DOC removal (inset) of HA by NCNT@GO-M retention and catalysis (b). Effluent-C and Effluent-R refer to the HA effluent after NCNT@GO-M catalysis and filtration, respectively.

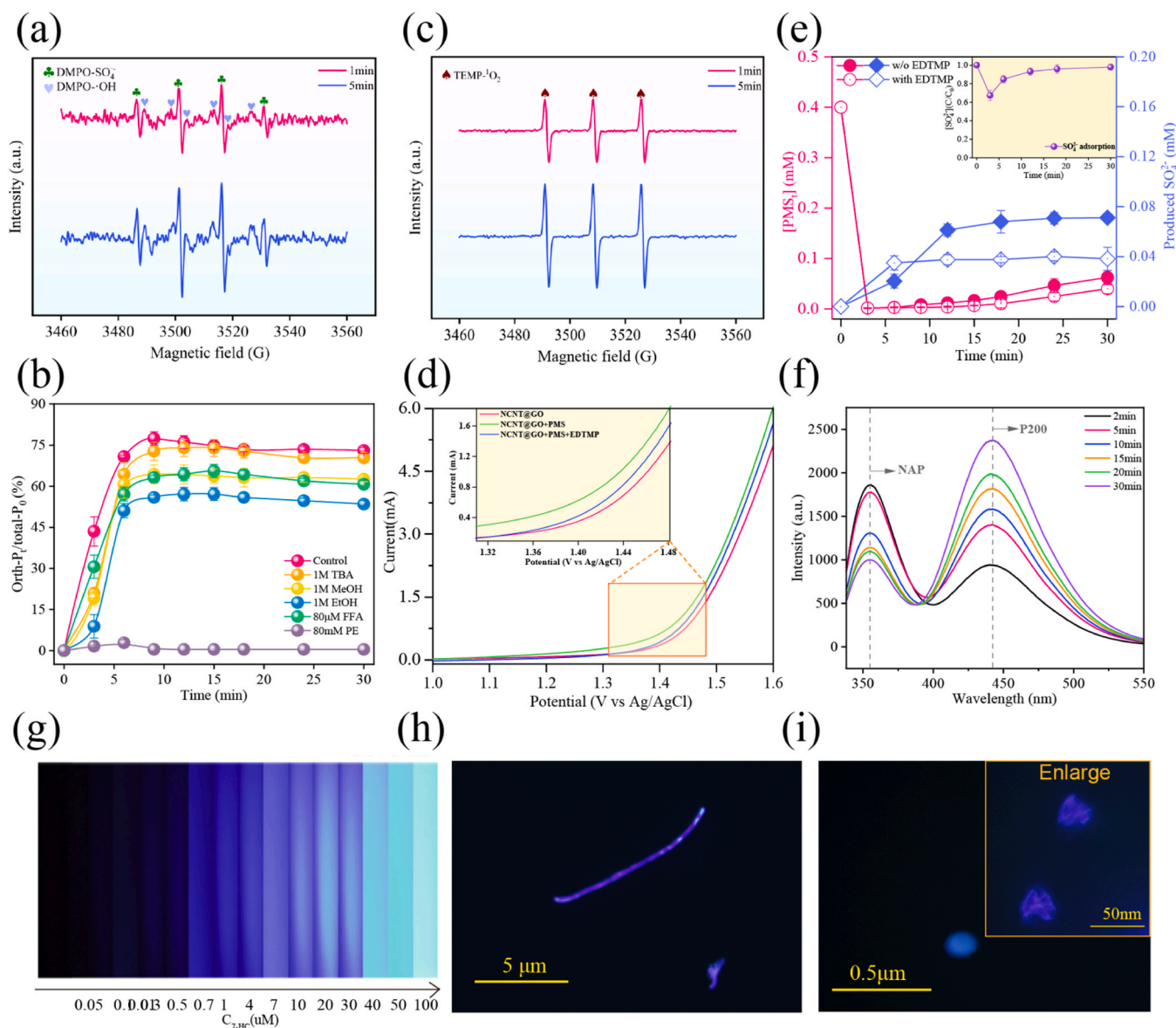


Fig. 5. (a) EPR spectra with DMPO as the trapping agents for radicals. (b) The effects of scavengers on Orth-P production. (c) EPR spectra with TEMP as the trapping agents for $^1\text{O}_2$. (d) LSV tests in different reaction systems. (e) PMS decomposition and SO_4^{2-} generation in different systems. (f) Steady-state fluorescence spectra of the NAP and P200 in NCNT@GO-M/PMS system. (g) Colorimetric references [29] of 7-HC solutions. Fluorescence microscopy images of the over view of (h) single NCNT, and (i) cross-sectional view of the discrete NCNT. Conditions: $[\text{EDTMP}]_0 = 50 \mu\text{M}$, $[\text{PMS}]_0 = 0.4 \text{ mM}$, without adjusting pH, $\text{TMP} = 0.2 \text{ bar}$, 0.4 mM of initial SO_4^{2-} for NCNT@GO-M adsorption experiment.

cannot be considered as a conclusive evidence for the existence of $^1\text{O}_2$, as reported, the TEMPO adduct signal may involve an electron-transfer mechanism. In such case, the catalyst [41] or [catalyst-oxidant]* complex [42] can extract one electron from TEMPO, resulting in the formation of TEMPO radical cation ($\text{TEMP}^{\bullet+}$), which reacted with molecular oxygen to generate $^1\text{O}_2$.

Furfuryl alcohol (FFA) ($k_{1\text{O}_2, \text{FFA}} = 1.2 \times 10^8 \text{ M}^{-1} \text{ s}^{-1}$) is a quencher for $^1\text{O}_2$. Fig. S10 indicated that excess FFA resulted in a 25% reduction in Orth-P generation. Nevertheless, this finding did not confirm that $^1\text{O}_2$ played a relatively important role for EDTMP degradation, given the higher reactivity of FFA with $\text{SO}_4^{\bullet-}$ and $\bullet\text{OH}$ relative to $^1\text{O}_2$ ($k_{\bullet\text{OH}, \text{FFA}} = 1.5 \times 10^{10} \text{ M}^{-1} \text{ s}^{-1}$, $k_{\text{SO}_4^{\bullet-}, \text{FFA}} = 1.3 \times 10^{10} \text{ M}^{-1} \text{ s}^{-1}$) [43]. Furthermore, high concentrations of FFA may compete with pollutants and disrupt the degradation process dominated by electron transfer mechanisms [44]. Thus, high concentrations of FFA often lead to an overestimation for the role of $^1\text{O}_2$ in quenching experiments. For these reasons, a lower concentration of FFA (80 μM) was selected to scavenge $^1\text{O}_2$. Fig. 5b showed

a negligible inhibition by FFA on Orth-P generation, suggesting that $^1\text{O}_2$ was also not the primary ROS responsible for EDTMP degradation. The result was consistent with Zhu et al.'s findings [45], where no Orth-P formation during the photosensitized rose bengal (RB) process to degrade phosphonates (a benchmark source of $^1\text{O}_2$). Wang et al. [43], also suggested that the contribution of $^1\text{O}_2$ to the majority of pollutants was negligible, as the second-order rate constants for the reaction of $^1\text{O}_2$ with pollutants were normally several orders of magnitude lower than those for $\bullet\text{OH}$ and $\text{SO}_4^{\bullet-}$, despite the concentrations of $^1\text{O}_2$ being 10^1 – 10^2 times higher than the $\text{SO}_4^{\bullet-}$ and $\bullet\text{OH}$. $^1\text{O}_2$ normally exhibits high selectivity toward electron-rich compounds, e.g., phenols [39]. Thus, $^1\text{O}_2$ is unlikely to be the major ROS in EDTMP degradation owing to the absence of lone electron pairs between carbon and phosphorus atoms, which makes it difficult for $^1\text{O}_2$ to break the C-P bond via electrophilic attack.

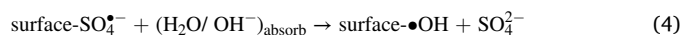
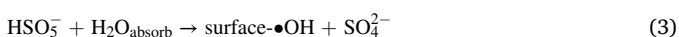
3.4.3. Probing electron transfer pathways

After excluding the main role of $^1\text{O}_2$, it is necessary to verify the electron transfer mechanism that TEMPO may be involved in. In electron transfer-dominated mechanism, pollutants act as electron donors, while electron acceptors exist as [catalyst-oxidant]* complex [46] or surface-activated oxidant [47], and oxidant cannot be decomposed by the catalyst without pollutants. Consequently, the electron transfer pathway was investigated through linear sweep voltammetry (LSV, Text S11) and PMS degradation tests, as shown in Figs. 5d-5e. Using NCNT@GO-M as the working electrode, the addition of PMS increased the current, suggesting that electron transfer existed between NCNT@GO-M and PMS, probably forming the complex, such as [NCNT-PMS]*, according to Ren et al. [46]. If electron transfer existed between the complex and EDTMP, the addition of EDTMP was expected to further increase the current. Nevertheless, Fig. 5d demonstrated a decrease in current intensity, indicating that EDTMP degradation does not involve electron transfer. Moreover, Fig. 5e revealed that PMS degradation surpassed 80% within a 30-minute reaction by NCNT@GO-M, with EDTMP addition marginally enhancing PMS decomposition. Thus, the electron transfer pathway can be excluded.

3.4.4. Probing surface-bound radicals

TBA and MeOH, as hydrophilic scavengers, have limited quenching effects on surface-bound radicals adsorbed on hydrophobic catalyst surfaces [48]. Ethanol (EtOH), a known scavenger for both $\bullet\text{OH}$ and $\text{SO}_4^{\bullet-}$ ($k_{\bullet\text{OH},\text{EtOH}} = (1.2\text{--}2.8) \times 10^9 \text{ M}^{-1} \text{ s}^{-1}$, $k_{\text{SO}_4^{\bullet-},\text{EtOH}} = (1.6\text{--}7.8) \times 10^7 \text{ M}^{-1} \text{ s}^{-1}$) [47], exhibits higher affinity towards the catalyst compared to that of MeOH [27], making it more effective in quenching surface-bound radicals. Therefore, EtOH was introduced into the NCNT@GO-M/PMS system, and a more significant inhibition on Orth-P generation compared to MeOH was observed (Fig. 5b). To further validate this hypothesis, Phenol (PE), serving as a quencher for surface-bound radicals [49], was added into the NCNT@GO-M/PMS system. As expected, Orth-P generation was nearly entirely inhibited. Further experiments (Fig. S11) confirmed that PE's quenching effect was due to the consumption of surface-bound radicals rather than competitive adsorption with PMS at the catalytic site, as the competitive adsorption would affect the activation and decomposition of PMS. Hence, it was established that surface-bound radicals were the primary mechanism for EDTMP degradation within the NCNT@GO-M/PMS system.

In the NCNT activation of PMS, electrons can migrate to the $\text{O}_{\text{II}}\text{-SO}_3^-$ part of PMS ($\text{H-O-I-O}_{\text{II}}\text{-SO}_3^-$) to produce $\bullet\text{OH}$ and $\text{SO}_4^{\bullet-}$ (Eq. (1)), or to the H-O-I moiety, resulting in $\text{SO}_4^{\bullet-}$ and OH^- (Eq. (2)) [50]. PMS decomposition primarily generates $\text{SO}_4^{\bullet-}$ at pH values from 3.0 to 7.0 [33]. To determine the major contribution of surface- $\text{SO}_4^{\bullet-}$ for EDTMP degradation, total $\text{SO}_4^{\bullet-}$ generation was measured, including $\text{SO}_4^{\bullet-}$ detected in the permeate and adsorbed on the NCNT@GO-M. Fig. 5e showed that PMS consumption was significantly greater than $\text{SO}_4^{\bullet-}$ production regardless of the presence of EDTMP, which was inconsistent with the stoichiometric relationship in Eq. 1. This result suggested that PMS decomposition involved the formation of surface- $\text{SO}_4^{\bullet-}$ and OH^- (Eq. (2)). Guan et al.'s group [51] recently developed a novel method for identifying and quantifying $\text{SO}_4^{\bullet-}$ in real-time, using naproxen (NAP) as an effective chemiluminescent probe, with the mechanism illustrated in Fig. S12. Thus, NAP was chosen to confirm the existence of surface- $\text{SO}_4^{\bullet-}$ in this NCNT@GO/PMS system (Text S12). The steady-state fluorescence spectra indicated a gradual increase in intensity over a 30-minute reaction time (Fig. 5f), indicating continuous surface- $\text{SO}_4^{\bullet-}$ generation. This result confirmed that surface- $\text{SO}_4^{\bullet-}$ plays a significant role in EDTMP degradation.



It should be noted that the carbon material/PMS system is a complex catalytic process, inevitably generating surface- $\bullet\text{OH}$, which should also be validated. Surface- $\bullet\text{OH}$ may be produced through two pathways in the NCNT@GO-M/PMS system: PMS oxidize adsorbed water molecules ($\text{H}_2\text{O}_{\text{adsorb}}$) on/near the catalyst (Eq. (3)) [52], or the generated surface- $\text{SO}_4^{\bullet-}$ react with $\text{H}_2\text{O}_{\text{adsorb}}$ and/or $\text{OH}^-_{\text{adsorb}}$ (Eq. (4)) ($k_{\text{SO}_4^{\bullet-},\text{H}_2\text{O}} \leq 5 \times 10^2 \text{ M}^{-1} \text{ s}^{-1}$, $k_{\text{SO}_4^{\bullet-},\text{OH}^-} = (4.6 \sim 6.5) \times 10^7 \text{ M}^{-1} \text{ s}^{-1}$) [53–55]. The former is thermodynamically impossible, as the redox potential of PMS ($\text{HSO}_5^-/\text{SO}_4^{\bullet-}$, 1.82 V_{NHE}) is lower than that of water ($\text{OH}^-/\text{H}_2\text{O}$, 2.8 V_{NHE}). Therefore, the existence of surface- $\bullet\text{OH}$ was likely resulted from the latter pathway (Eq. (4)). To explore the presence of surface- $\bullet\text{OH}$, coumarin served as a probe was added to the counterpart NCNT@GO-P/PMS heterogeneous system (Text S13). Non-fluorescent coumarin can be quantitatively transformed by $\bullet\text{OH}$ into fluorescent 7-hydroxycoumarin (7-HC), which can be observed using a fluorescent microscope even at very low concentrations [42], with the reaction mechanism depicted in Fig. S13a. Fig. 5g presented the standard colorimetric reference for 7-HC solution with the concentration range from 0.01 to 500 μM , as referenced from the literature [29]. The luminous color of 7-HC indicated the concentration below 1 μM (Figs. 5h-5i). To verify the generation of surface- $\bullet\text{OH}$ in the NCNT@GO/PMS system through the reaction of Eq. (4), an additional fluorescence experiment was performed by adjusting the pH to 8.5 according to Wang et al. [53]. The cyan-colored region indicated that the tubular NCNT was surrounded by higher concentrations of surface- $\bullet\text{OH}$ (Fig. S13c-13e). As a result, PMS decomposition mainly generated surface- $\text{SO}_4^{\bullet-}$, with a fraction of the surface- $\text{SO}_4^{\bullet-}$ being converted into surface- $\bullet\text{OH}$.

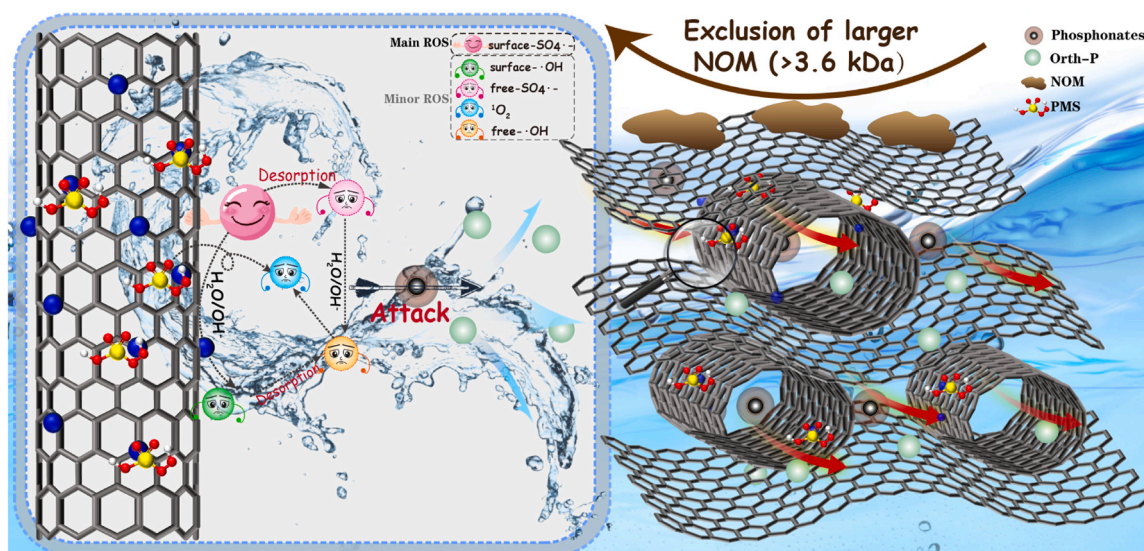
Based on the above discussion, a catalytic mechanism is proposed for the activation of PMS and the degradation of EDTMP to produce Orth-P (Scheme 1). Initially, the negatively charged PMS is adsorbed onto the graphitic N sites of the NCNT catalyst, which is crucial for the catalytic reaction [52]. Subsequently, this adsorption process facilitates electron transfer to PMS, cleaving the O-O bond and primarily generating surface- $\text{SO}_4^{\bullet-}$. A small portion of surface- $\text{SO}_4^{\bullet-}$ reacts with H_2O and OH^- on the NCNT surface to form surface- $\bullet\text{OH}$, while a minor amount of $^1\text{O}_2$ is generated through PMS oxidation over the electron-deficient carbon atoms neighboring graphitic N [56]. The adsorbed surface radicals then detach from the catalyst surface, forming free radicals. Finally, the primary surface- $\text{SO}_4^{\bullet-}$ and secondary ROS, including surface- $\bullet\text{OH}$, free- $\text{SO}_4^{\bullet-}/\bullet\text{OH}$ and $^1\text{O}_2$, contribute to the degradation of EDTMP to Orth-P.

3.5. Mechanistic insights into enhanced kinetics by NCNT@GO-M

Surface-bound radicals primarily oxidize the target pollutants at the catalyst surface and/or the solid-liquid interface region, rather than in the bulk phase [25]. Therefore, the reaction kinetics of EDTMP in the NCNT@GO-M catalytic system can be enhanced by the enrichment of $\text{SO}_4^{\bullet-}$ at the surface/interface of NCNT and the enhanced mass transfer rate of EDTMP from the bulk solution to the reaction region.

3.5.1. Surface- $\text{SO}_4^{\bullet-}$ enrichment effect

Spatial confinement can increase local ROS concentration due to short diffusion distance [57], thus $\text{SO}_4^{\bullet-}$ was enriched on the NCNT surface/interface within the nanoconfined NCNT@GO-M. A rough estimation (Text S14) indicated that the diffusion distance of surface- $\text{SO}_4^{\bullet-}$ was much greater than the pore size of NCNT@GO-M (1.60 nm) (Fig. S14). By simulating the distribution of surface- $\text{SO}_4^{\bullet-}$ as a function of the distance from the active sites, it was determined that 50% of surface- $\text{SO}_4^{\bullet-}$ was consumed at $\sim 300 \text{ nm}$ away from the surface. Consequently, it could be speculated that the EDTMP degradation occurred in regions where the concentration of surface- $\text{SO}_4^{\bullet-}$ was relatively high.



Scheme 1. Mechanism diagram.

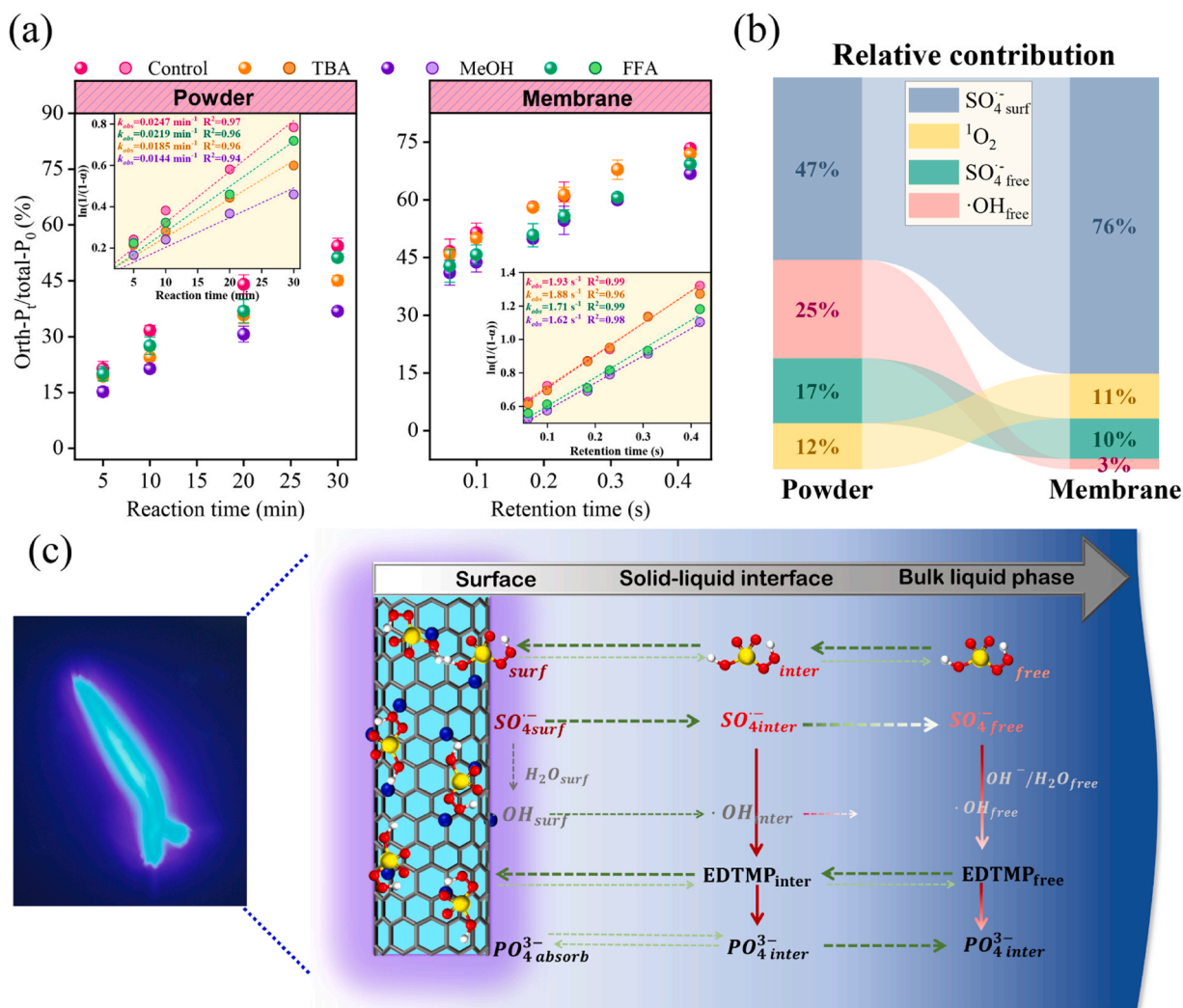


Fig. 6. Effects of different quenchers on Orth-P production in NCNT@GO-P system (Powder, left) and NCNT@GO-M system (Membrane, right) (a). The inset figures show the k_{obs} of Orth-P production, all $R^2 > 0.9$. The relative contribution of involved reactive species in NCNT@GO-P and NCNT@GO-M system (b). Reaction schematic depicting the heterogeneous catalytic model (c). Conditions: $[PMS]_0 = 0.4$ mM, $[EDTMP]_0 = 50$ μ M, $[TBA] = [MeOH] = 400$ mM, $[FFA] = 80$ μ M, without adjusting PH, NCNT@GO-P = 40 mg L⁻¹; TMP = 0–2.0 bar for membrane filtration tests.

3.5.2. Enhanced mass transfer effect

Compared to traditional heterogeneous catalysis, membrane catalysis demonstrates enhanced reaction kinetics due to pressure-driven effects. To further investigate the influence of nanoconfinement induced by GO-laminates on EDTMP mass transfer, a semi-empirical Sherwood correlation approach [58], was used to calculate the mass transfer coefficients of EDTMP (k_m) in NCNT@GO-M and NCNT-M system (Text S15). Table S5 indicated that the k_m in the nanoconfined NCNT@GO-M system reached $1.59 \times 10^{-3} \text{ m} \cdot \text{s}^{-1}$, almost 1.9 times greater than in the non-confined NCNT-M system ($8.49 \times 10^{-4} \text{ m} \cdot \text{s}^{-1}$). As reported, organic molecules contained in ultrasmall nanospaces ($< 2 \text{ nm}$) enable their structures to transform from a disordered arrangement to an ordered highly mobile state [59]. The ordered structure can eliminate diffusion limitations and facilitate the proximity of organic to reactive sites [60]. In this study, the inner diameter of NCNT is around 20–30 nm, which is much larger than the hydrated ions. Consequently, EDTMP and water molecules in the solution are likely to pass through NCNT's outer channels (the outer surface of its curved walls) in a disordered manner [61]. In contrast, the nanochannels of NCNT@GO-M are only 1.60 nm ($< 2 \text{ nm}$) leading to a larger slip length of water molecules inside graphene capillaries, thus the transport kinetics of EDTMP is improved [62]. The NCNT-M (3.09 nm) and NCNT@GO-M (2.50 nm) exhibited different thicknesses. Nevertheless, the difference in mass transfer caused by membrane thickness was negligible compared to the confinement effect (Text S15, Table S5).

3.5.3. Surface- $\text{SO}_4^{\bullet-}$ contribution

The impact of confinement effect on surface-bound radicals remains unclear, although it is generally believed to enhance the utilization of short-lived free radicals (e.g., free $\text{SO}_4^{\bullet-}$ and $\bullet\text{OH}$) [63]. By analyzing the degradation kinetics of EDTMP in both the nanoconfined NCNT@GO-M and the traditional unconfined NCNT@GO-P heterogeneous system (Fig. 6a), the relative contribution of involved reactive species was evaluated, including surface- $\text{SO}_4^{\bullet-}$, free- $\text{SO}_4^{\bullet-}$, free- $\bullet\text{OH}$ and $^1\text{O}_2$ (detailed calculations in Text S8). Fig. 6b and Table S6 demonstrated that both the NCNT@GO-P and NCNT@GO-M catalytic systems involved the surface- $\text{SO}_4^{\bullet-}$ oxidation pathway, nevertheless, there was a significant difference in their relative contribution. In the NCNT@GO-M catalytic system, surface- $\text{SO}_4^{\bullet-}$ oxidation accounted for 76%, markedly higher than in the NCNT@GO-P system (47%). Accordingly, the total oxidation contribution of free radicals ($\bullet\text{OH}$ and $\text{SO}_4^{\bullet-}$) in the NCNT@GO-M catalytic system was only 13%, significantly lower than the 42% observed in the NCNT@GO-P catalytic system. Overall, the confinement effect in the NCNT@GO-M system significantly enhanced the relative contribution of surface- $\text{SO}_4^{\bullet-}$.

3.5.4. Proposed surface radicals-dominated catalytic model

Diffusion is considered the primary driving force within the NCNT@GO-P heterogeneous system. In membrane filtration processes (NCNT-M and NCNT@GO-M), both diffusion and pressure-driven mass transfer mechanisms contribute to the catalytic reaction, while the confinement effect within NCNT@GO-M further amplifies mass transfer. A heterogeneous catalytic model based on surface-bound radicals was established (Fig. 6c). This model was developed based on fluorescence visualization of the spatial distribution of surface-bound radicals (Fig. S13), and includes the surface, solid-liquid interface, and bulk liquid phases.

(I) Migration and activation of PMS on catalyst surfaces and interfaces

Firstly, PMS diffuses from the liquid phase to the interface and catalyst surface, and attaches to the catalytic sites. Subsequently, the catalytic sites on the NCNT surface transfer electrons to the adsorbed PMS, generating surface- $\text{SO}_4^{\bullet-}$ and minor surface- $\bullet\text{OH}$. The mass transfer efficiency of PMS, similar to EDTMP, followed the order of NCNT@GO-M > NCNT-M > NCNT@GO-P due to pressure-driven and confinement effects. Consequently, this leads to a higher efficiency in activating PMS

to generate more surface- $\text{SO}_4^{\bullet-}/\bullet\text{OH}$ within the NCNT@GO-M system. These surface- $\text{SO}_4^{\bullet-}/\bullet\text{OH}$ species then diffuse to the interface layer, forming interface- $\text{SO}_4^{\bullet-}/\bullet\text{OH}$. The diffusion equilibrium of $\text{SO}_4^{\bullet-}/\bullet\text{OH}$ between the surface and interface layer is ignored considering their rapid reaction with EDTMP, making the re-adsorption of $\text{SO}_4^{\bullet-}/\bullet\text{OH}$ from the interface layer to the surface negligible.

(II) Migration and degradation of EDTMP on catalyst surfaces and interfaces

The diffusion of EDTMP from the bulk phase to the interface and surface initiates catalytic reactions. In the interface layer, the oxidation of EDTMP occurs through a bidirectional migration process, with EDTMP migrating to the interface and surface- $\text{SO}_4^{\bullet-}/\bullet\text{OH}$ diffusing to this region. Subsequently, EDTMP transports to the surface and interacts with surface-bound radicals. The accelerated transfer of EDTMP in the NCNT@GO-M system to the surface/interface reaction site allows it to capture more surface- $\text{SO}_4^{\bullet-}$, thus enhancing the availability of surface- $\text{SO}_4^{\bullet-}$.

(III) Transformation of surface- $\text{SO}_4^{\bullet-}$ and free- $\text{SO}_4^{\bullet-}$ in the liquid phase

Surface- $\text{SO}_4^{\bullet-}$ has a longer half-life span (57.2 μs) compared to free radicals (1 μs for $\bullet\text{OH}$ and 30–40 μs for $\text{SO}_4^{\bullet-}$) [28], facilitating diffusion over greater distances. It is assumed that surface- $\text{SO}_4^{\bullet-}$ transfer to the bulk phase, forming free- $\text{SO}_4^{\bullet-}$ to oxidize EDTMP ($k_{\text{SO}_4^{\bullet-}, \text{phosphonates}} = (2.9 \sim 7.7) \times 10^7 \text{ M}^{-1} \text{ s}^{-1}$) [64]. Partial free- $\text{SO}_4^{\bullet-}$ react with $\text{H}_2\text{O}/\text{OH}^-$ in the bulk phase ($k_{\text{SO}_4^{\bullet-}, \text{H}_2\text{O}} \leq 5 \times 10^2 \text{ M}^{-1} \text{ s}^{-1}$, $k_{\text{SO}_4^{\bullet-}, \text{OH}^-} = (4.6 \sim 6.5) \times 10^7 \text{ M}^{-1} \text{ s}^{-1}$), generating free- $\bullet\text{OH}$ for EDTMP oxidation ($k_{\text{OH}, \text{phosphonates}} = (1.1 \sim 6.8) \times 10^8 \text{ M}^{-1} \text{ s}^{-1}$) [53,64–66]. In the NCNT@GO-P catalytic system, diffusion plays a major driving force, and the diffusion rate of radical species from the surface to the liquid phase ($\sim 2.3 \times 10^{-9} \text{ m}^2 \text{ s}^{-1}$) [26] being faster than that of EDTMP from the liquid phase to the surface ($6.66 \times 10^{-10} \text{ m}^2 \text{ s}^{-1}$, Text S15). Hence, surface- $\text{SO}_4^{\bullet-}$ is likely to preferentially diffuse to the liquid phase and be transformed into free- $\text{SO}_4^{\bullet-}/\bullet\text{OH}$, enhancing the contribution of free radicals to EDTMP oxidation. In the NCNT@GO-M catalytic system, the confinement effect limits the diffusion of surface- $\text{SO}_4^{\bullet-}$, while pressure-driven mechanism and confinement effect together enhance the mass transfer of EDTMP to the catalyst's surface enriched with surface- $\text{SO}_4^{\bullet-}$, thereby significantly enhancing the contribution of surface- $\text{SO}_4^{\bullet-}$ to EDTMP oxidation.

3.6. Potential applicability

3.6.1. Reusability

The reusability of the catalytic membrane, a critical factor for practical use, was investigated through five cycles tests of EDTMP degradation in the NCNT@GO-M/PMS system. NCNT@GO-M maintained its catalytic efficiency over the first four cycles with a slight decrease of 5.3%, but a moderate decrease of 30.2% after five cycles (Fig. 7a). This excellent stability stems from the uniform distribution of NCNT within the GO-laminate, avoiding the aggregation of NCNT and protecting them from deactivation [67]. The catalytic activity decreased after four cycles, probably due to the accumulation of oxidation intermediates of EDTMP on the catalyst surface, which hindered the interaction between the catalytic site and PMS.

3.6.2. Environmental factors

The impact of different pH, anions and real waters on EDTMP degradation were investigated. The effect of pH was investigated by varying the initial pH from 3.5 to 11.0. As shown in Fig. 7b, Orth-P production was significantly inhibited at strong alkaline conditions (pH = 11.0), which was attributed to the reduction of $\text{SO}_4^{\bullet-}$ concentration (Eq. 4), as reported by Wang et al. [53]. In general, the NCNT@GO-M/PMS system can effectively degrade EDTMP to Orth-P over a wider pH range.

Fig. 7c showed that the presence of Cl^- , NO_3^- and HCO_3^- had a negligible impact on EDTMP degradation to Orth-P in the NCNT@GO-

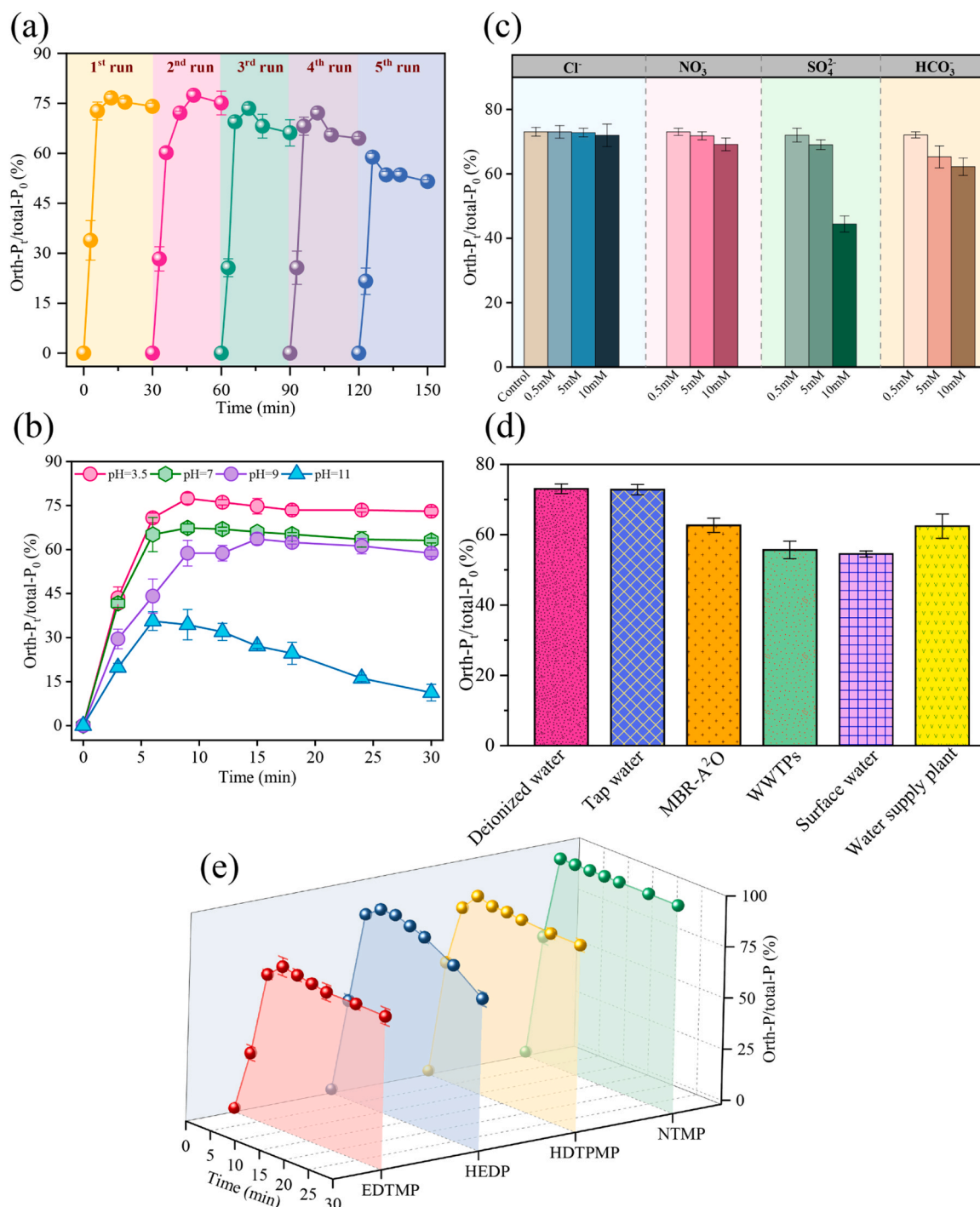


Fig. 7. Reusability tests on NCNT@GO-M (a); Effects of background anions (b), solution pH (c) and real waters (d) on EDTMP degradation to Orth-P by NCNT@GO-M/PMS system. Degradation efficiency of different phosphonates compounds in NCNT@GO-M/PMS system (e) Conditions: $[phosphonates]_0 = 50 \mu M$, $[PMS]_0 = 0.4 \text{ mM}$, $TMP = 0.2 \text{ bar}$, without adjusting pH.

M/PMS system, contrasting with the significant inhibition in traditional homogeneous and heterogeneous AOPs [45,68]. This inhibition is primarily attributed to the futile consumption of free radicals ($\bullet OH$ and $SO_4^{\bullet -}$) [68], or their coordination with metal catalysts [45], which leads to a reduction of reactive intermediates. For NCNT@GO-M/PMS system, the surface-radicals were confined within the pores and a low affinity for hydrophilic anions with the NCNT's surface due to the hydrophobic properties of the N dopant [69], minimizing the inhibition of anions. A relatively significant inhibition was observed with 10 mM of SO_4^{2-} , which could be attributed to the high concentration of SO_4^{2-} reducing the redox

potential of $SO_4^{\bullet -}/SO_4^{2-}$, thereby affecting PMS activation [70].

The NCNT@GO-M/PMS system was tested using five real waters (Table S7) for EDTMP degradation, and Fig. 7d demonstrated excellent degradation efficiency in various scenarios. Such superior anti-interference ability can be ascribed to the size exclusion effect, as discussed in Section 3.3. Additionally, radicals adsorbed on hydrophobic catalyst's surfaces exhibited higher selectivity and less affected by the water matrices than their free counterparts [42]. This resulted in although low-MW NOM penetrating into the membrane pores, the hydrophilic components within this fraction was difficult to consume the

surface-radicals on the hydrophobic surface. This unique design of the membrane structure significantly improves the anti-interference ability.

3.6.3. Universality

The currently reported AOPs often exhibit unsatisfactory degradation efficiency for some phosphonates with complex structures [71]. By contrast, the NCNT@GO-M/PMS system effectively degraded various

phosphonates (Fig. 7e), with detailed molecular structures in Table S3. Given that the molecular sizes of these phosphonates (calculated using Stokes-Einstein equation, Text S9) are smaller than the membrane pore size, they can permeate into the pores and react with the catalytic sites. The non-selective and strong oxidative surface-SO₄^{•−} can attack C-P bonds indiscriminately, enhancing the degradation/transformation of a wide range of phosphonates.

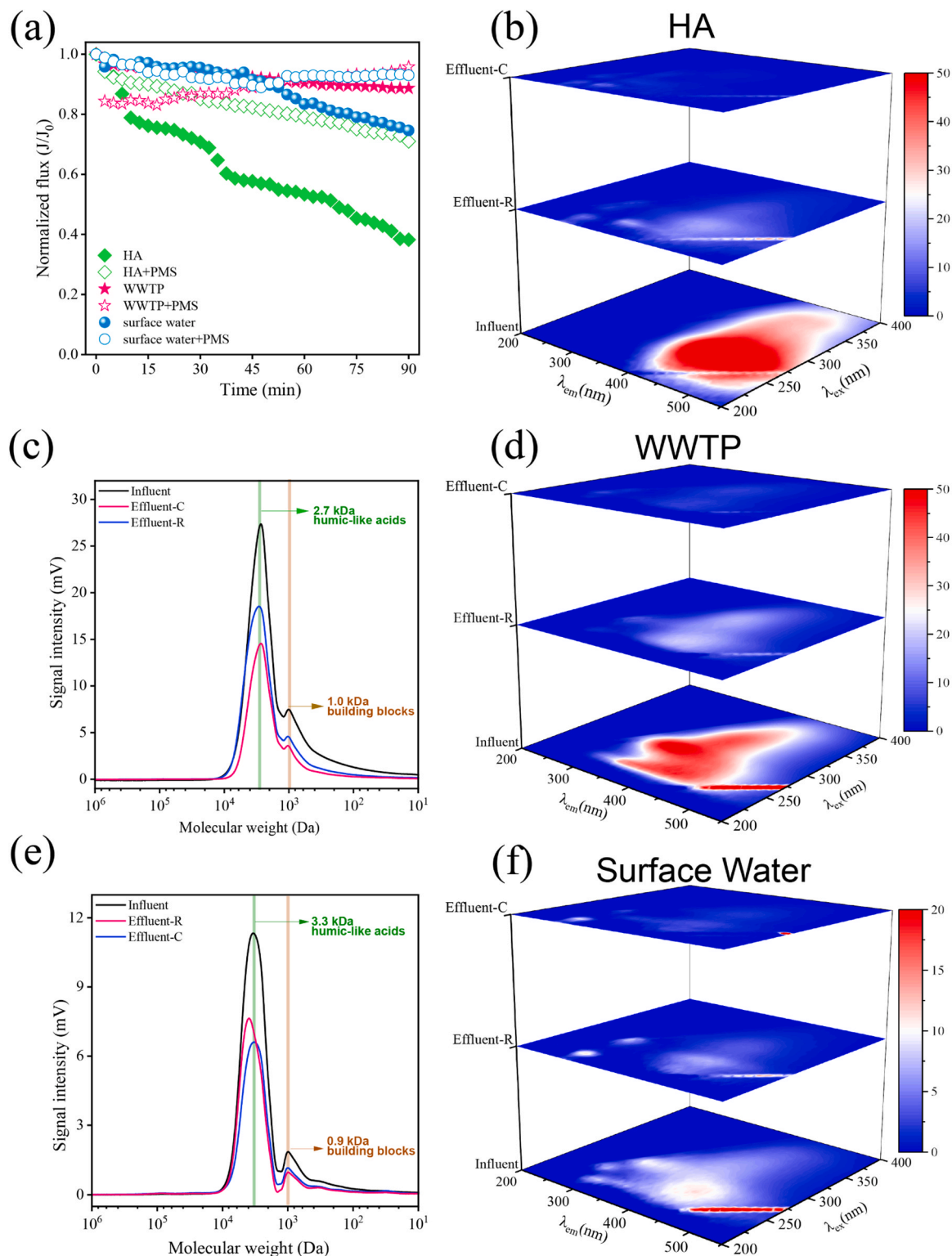


Fig. 8. (a) Normalized flux curves during fouling control experiments. The SEC spectra of (b) WWTPs effluent and (c) surface water. The fluorescence EEM spectra of (d) HA, (e) WWTPs effluent and (f) surface water.

3.6.4. Antifouling and self-cleaning performance

To evaluate the antifouling and self-cleaning performance of NCNT@GO-M, dynamic fouling experiments were conducted using HA (5 mg·C L⁻¹) as a representative organic foulant. The normalized flux of NCNT@GO-M dropped to 0.38 within a 90-minute filtration (Fig. 8a), evidencing that significant fouling occurred. This was ascribed to the MW of HA (~4.5 kDa, Fig. 4b) larger than that of membrane pores (3.6 kDa, calculated through PEG interception method [72]), leading to HA retention and deposition on the membrane surface or within the pores. The flux decline was obviously alleviated by adding PMS (Fig. 8a), showing excellent self-cleaning property of NCNT@GO-M/PMS. This was attributed to the superior catalytic activity of the NCNT@GO-M/PMS system, which generated ROS facilitating the decomposition of HA deposited on membrane into smaller organics (~2.8 kDa, Fig. 4b). Furthermore, the results of 3D-EEM confirmed the retention and catalytic effectiveness for HA by NCNT@GO-M, with a significant reduction in fluorescence intensity after filtration and catalysis, indicating the effective capture and decomposition for HA molecules by NCNT@GO-M.

The antifouling ability of NCNT@GO-M was assessed in real waters, including surface water and WWTP effluent. As shown in Fig. 8a, the normalized flux of the both samples remained stable for up to 90 min. The SEC curves (Fig. 8c and Fig. 8e) exhibited the presence of medium-MW humic-like substances (2.7 kDa in WWTP effluent and 3.3 kDa in surface water) and low-MW building blocks (1.0 kDa and 0.9 kDa), which were more easily to pass through the membrane pores, reducing fouling potential. Notably, surface water experienced more severe fouling than WWTP effluent due to the humic-like acids (3.3 kDa) in the former closer to the pore size (3.6 kDa), leading to their easier accumulation within membrane pores causing pore blocking after a long period of operation. The addition of PMS alleviated fouling, maintaining the normalized flux above 0.9 after 90 min. Additionally, fluorescent substances in the both samples were also effectively removed through membrane filtration and catalysis (Fig. 8d and Fig. 8f). In conclusion, NCNT@GO-M exhibited superior antifouling and self-cleaning performance in real waters.

4. Conclusion

In summary, we aimed to transform organic phosphonates into P-nutrients by constructing a LNCM characterized by high permeability and efficient catalytic activity. The unique merits of NCNT@GO-M lies in the intercalation of NCNT, which exploits a surface-bound radical-dominated oxidation pathway and reinforce the benefits of nano-confinement, thereby improving the utilization of surface-SO₄^{•-} by EDTMP, as demonstrated by mass transfer kinetics studies. The NCNT@GO-M/PMS catalytic system achieves Ortho-P production rate up to 75% with a retention time of approximately 0.45 s, equivalent to a permeation flux of 21.5 L m⁻² h⁻¹. Additionally, it enhances membrane permeability, potentially reduce energy consumption, and minimizes biological risks. The lower oxidant/catalyst dosage, ultra-thin catalytic layer, excellent degradation efficiency, ultrafast reaction kinetics, and outstanding antifouling ability all highlight the superiority of the NCNT@GO-M's structure. Furthermore, the NCNT@GO-M/PMS catalytic system exhibits outstanding Ortho-P transformation performance in various real water matrix. It provides an effective strategy for the degradation of organic phosphonates in wastewater, while also offering a new perspective for the direct reuse of wastewater, which is more feasible compared with traditional heterogeneous catalytic system, as the latter faces challenges in catalyst recovery and regeneration.

CRediT authorship contribution statement

Qiushan Liu: Methodology, Formal analysis. **Tong Zhou:** Methodology, Formal analysis. **Yufei Wang:** Visualization, Software. **Kemeng Du:** Formal analysis, Data curation. **Jin Guo:** Writing – review &

editing, Supervision, Resources, Project administration, Funding acquisition, Conceptualization. **Na Wei:** Methodology, Data curation. **Guohan Liu:** Methodology, Formal analysis. **Wenjun Wu:** Writing – original draft, Methodology, Investigation, Data curation.

Declaration of Competing Interest

The authors declare that they have no known competing financial interests or personal relationships that could have appeared to influence the work reported in this paper.

Data availability

No data was used for the research described in the article.

Acknowledgements

This work was supported by the National Natural Science Foundation of China (Grant No. 51778014) and the Beijing Nova Programme China (Grant No. Z1511000003150139).

Appendix A. Supporting information

Supplementary data associated with this article can be found in the online version at doi:10.1016/j.apcatb.2024.124118.

References

- [1] R. Altaf, B. Sun, H. Lu, H. Zhao, D. Liu, Removal and recovery of phosphonates from wastewater via adsorption, *Crit. Rev. Environ. Sci. Technol.* 53 (2022) 1032–1058.
- [2] Y. Ren, W. Zheng, X. Duan, N. Goswami, Y. Liu, Recent advances in electrochemical removal and recovery of phosphorus from water: a review, *Environ. Funct. Mater.* 1 (2022) 10–20.
- [3] Y. Zhao, X. Tong, Y. Chen, Fit-for-purpose design of nanofiltration membranes for simultaneous nutrient recovery and micropollutant removal, *Environ. Sci. Technol.* 55 (2021) 3352–3361.
- [4] Y. Jia, S. Sun, S. Wang, X. Yan, J. Qian, B. Pan, Phosphorus in water: a review on the speciation analysis and species specific removal strategies, *Crit. Rev. Environ. Sci. Technol.* (2022) 1–22.
- [5] K. Venkiteshwaran, P.J. McNamara, B.K. Mayer, Meta-analysis of non-reactive phosphorus in water, wastewater, and sludge, and strategies to convert it for enhanced phosphorus removal and recovery, *Sci. Total Environ.* 644 (2018) 661–674.
- [6] E. Rott, H. Steinmetz, J.W. Metzger, Organophosphonates: a review on environmental relevance, biodegradability and removal in wastewater treatment plants, *Sci. Total Environ.* 615 (2018) 1176–1191.
- [7] S. Wang, B. Zhang, C. Shan, X. Yan, H. Chen, B. Pan, Occurrence and transformation of phosphonates in textile dyeing wastewater along full-scale combined treatment processes, *Water Res.* 184 (2020) 116173.
- [8] G. Adam, A. Mottet, S. Lemaigre, B. Tsachidou, E. Trouvé, P. Delfosse, Fractionation of anaerobic digestates by dynamic nanofiltration and reverse osmosis: an industrial pilot case evaluation for nutrient recovery, *J. Environ. Chem. Eng.* 6 (2018).
- [9] C. Blöcher, C. Niewersch, T. Melin, Phosphorus recovery from sewage sludge with a hybrid process of low pressure wet oxidation and nanofiltration, *Water Res.* 46 (2012) 2009–2019.
- [10] T. Zhu, X. Li, X. Zhu, B. Liu, J. Zhu, J. Luo, Critical review of catalysis-assisted nanofiltration for micropollutants removal: catalytic coupled nanofiltration system vs catalytic nanofiltration membrane, *Crit. Rev. Environ. Sci. Technol.* (2022) 1–23.
- [11] C. Zhao, B. Liu, T. Zhu, X. Zhu, X. Cheng, Mechanistic insight into single-atom Fe loaded catalytic membrane with peracetic acid and visible light activation, *J. Hazard Mater.* 460 (2023) 132506.
- [12] Z. Bai, S. Gao, H. Yu, X. Liu, J. Tian, Layered metal oxides loaded ceramic membrane activating peroxymonosulfate for mitigation of NOM membrane fouling, *Water Res.* 222 (2022) 118928.
- [13] S. Zhang, T. Hedtko, Q. Zhu, M. Sun, S. Weon, Y. Zhao, E. Stavitski, M. Elimelech, J. H. Kim, Membrane-confined iron oxychloride nanocatalysts for highly efficient heterogeneous fenton water treatment, *Environ. Sci. Technol.* 55 (2021) 9266–9275.
- [14] B. Liu, Z. Xue, Z. Wu, H. Zeng, C. Zhao, L. Deng, Z. Shi, Layer-by-layer-assembled loose nanofiltration membrane for persulfate activity enhancement: performance and process regulation, *ACS EST Water* 2 (2022) 1614–1624.
- [15] Q. Zhang, S. Chen, X. Fan, H. Zhang, H. Yu, X. Quan, A multifunctional graphene-based nanofiltration membrane under photo-assistance for enhanced water

- treatment based on layer-by-layer sieving, *Appl. Catal. B: Environ.* 224 (2018) 204–213.
- [16] J. Zhu, J. Wang, A.A. Uliana, M. Tian, Y. Zhang, Y. Zhang, A. Volodin, K. Simoons, S. Yuan, J. Li, J. Lin, K. Bernaerts, B. Van der Bruggen, Mussel-inspired architecture of high-flux loose nanofiltration membrane functionalized with antibacterial reduced graphene oxide-copper nanocomposites, *ACS Appl. Mater. Interfaces* 9 (2017) 28990–29001.
 - [17] J. Ye, J. Dai, D. Yang, C. Li, Y. Yan, 1D/2D nanoconfinement Fe₃O₄ and nitrogen-doped carbon matrix for catalytic self-cleaning membranes removal for pollutants, *J. Environ. Chem. Eng.* 9 (2021).
 - [18] J. Ye, Y. Wang, Z. Li, D. Yang, C. Li, Y. Yan, J. Dai, 2D confinement freestanding graphene oxide composite membranes with enriched oxygen vacancies for enhanced organic contaminants removal via peroxymonosulfate activation, *J. Hazard Mater.* 417 (2021) 126028.
 - [19] X. Wu, K. Rigby, D. Huang, T. Hedtke, X. Wang, M.W. Chung, S. Weon, E. Stavitski, J.H. Kim, Single-atom cobalt incorporated in a 2D graphene oxide membrane for catalytic pollutant degradation, *Environ. Sci. Technol.* 56 (2022) 1341–1351.
 - [20] W. Zhang, S. Zhang, C. Meng, Z. Zhang, Nanoconfined catalytic membranes assembled by cobalt-functionalized graphitic carbon nitride nanosheets for rapid degradation of pollutants, *Appl. Catal. B-Environ.* 322 (2023).
 - [21] Y. Han, Y. Jiang, C. Gao, High-flux graphene oxide nanofiltration membrane intercalated by carbon nanotubes, *ACS Appl. Mater. Interfaces* 7 (2015) 8147–8155.
 - [22] W.-L. Jiang, M.R. Haider, J.-L. Han, Y.-C. Ding, X.-Q. Li, H.-C. Wang, H.M. Adeel Sharif, A.-J. Wang, N.-Q. Ren, Carbon nanotubes intercalated RGO electro-Fenton membrane for coenhanced permeability, rejection and catalytic oxidation of organic micropollutants, *J. Membr. Sci.* 623 (2021).
 - [23] W. Jiang, M.R. Haider, Y. Duan, J. Han, Y. Ding, B. Mi, A. Wang, Metal-free electrified membranes for contaminants oxidation: synergy effect between membrane rejection and nanoconfinement, *Water Res* 248 (2023) 120862.
 - [24] H. Ma, G. Wang, Z. Xu, X. Dong, X. Zhang, Confining peroxymonosulfate activation in carbon nanotube intercalated nitrogen doped reduced graphene oxide membrane for enhanced water treatment: the role of nanoconfinement effect, *J. Colloid Interface Sci.* 608 (2022) 2740–2751.
 - [25] Y. Chen, C.J. Miller, T.D. Waite, Heterogeneous Fenton chemistry revisited: mechanistic insights from ferrihydrite-mediated oxidation of formate and oxalate, *Environ. Sci. Technol.* 55 (2021) 14414–14425.
 - [26] S. Zhang, M. Sun, T. Hedtke, A. Deshmukh, X. Zhou, S. Weon, M. Elimelech, J.-H. Kim, Mechanism of heterogeneous fenton reaction kinetics enhancement under nanoscale spatial confinement, *Environ. Sci. Technol.* 54 (2020) 10868–10875.
 - [27] R. Xie, K. Guo, Z. Ao, Z. Suo, H. Huang, D.Y.C. Leung, Surface-bound radicals generated from cobalt single-atom catalyst: mechanism of boosting Fenton-like reactions, *Chem. Eng. J.* (2023) 461.
 - [28] C. Chen, M. Yan, Y. Li, Y. Hu, J. Chen, S. Wang, X.-L. Wu, X. Duan, Single-atom co sites confined in layered double hydroxide for selective generation of surface-bound radicals via peroxymonosulfate activation, *Appl. Catal. B: Environ.* 340 (2024).
 - [29] S. Zhang, X. Quan, J.F. Zheng, D. Wang, Probing the interphase "HO zone" originated by carbon nanotube during catalytic ozonation, *Water Res* 122 (2017) 86–95.
 - [30] X. Duan, H. Sun, J. Kang, Y. Wang, S. Indrawirawan, S. Wang, Insights into Heterogeneous catalysis of persulfate activation on dimensional-structured nanocarbons, *ACS Catal.* 5 (2015) 4629–4636.
 - [31] X. Duan, C. Su, L. Zhou, H. Sun, A. Suvorova, T. Odedairo, Z. Zhu, Z. Shao, S. Wang, Surface controlled generation of reactive radicals from persulfate by carbocatalysis on nanodiamonds, *Appl. Catal. B: Environ.* 194 (2016) 7–15.
 - [32] X. Duan, Z. Ao, H. Sun, L. Zhou, G. Wang, S. Wang, Insights into N-doping in single-walled carbon nanotubes for enhanced activation of superoxides: a mechanistic study, *Chem. Commun. (Camb.)* 51 (2015) 15249–15252.
 - [33] X. Wang, Y. Qin, L. Zhu, H. Tang, Nitrogen-doped reduced graphene oxide as a bifunctional material for removing bisphenols: synergistic effect between adsorption and catalysis, *Environ. Sci. Technol.* 49 (2015) 6855–6864.
 - [34] Y. Wang, N. Wei, J. Zeng, Y. Wu, T. Zhou, G. Liu, Q. Liu, J. Guo, Nitrogen-doped carbon nanotube modified ultrafiltration membrane activating peroxymonosulfate for catalytic transformation of phosphonate and mitigation of membrane fouling, *Sep. Purif. Technol.* 314 (2023).
 - [35] W.-J. Zeng, C. Li, Y. Feng, S.-H. Zeng, B.-X. Fu, X.-L. Zhang, Carboxylated multi-walled carbon nanotubes (MWCNTs-COOH)-intercalated graphene oxide membranes for highly efficient treatment of organic wastewater, *J. Water Process Eng.* 40 (2021).
 - [36] Y. Liu, Q. Lin, Y. Guo, J. Zhao, X. Luo, H. Zhang, G. Li, H. Liang, The nitrogen-doped multi-walled carbon nanotubes modified membrane activated peroxymonosulfate for enhanced degradation of organics and membrane fouling mitigation in natural waters treatment, *Water Res* 209 (2021) 117960.
 - [37] M. Ateia, O.G. Apul, Y. Shimizu, A. Muflihah, C. Yoshimura, T. Karanfil, Elucidating adsorptive fractions of natural organic matter on carbon nanotubes, *Environ. Sci. Technol.* 51 (2017) 7101–7110.
 - [38] J. Miao, W. Geng, P.J.J. Alvarez, M. Long, 2D N-doped porous carbon derived from polydopamine-coated graphitic carbon nitride for efficient nonradical activation of peroxymonosulfate, *Environ. Sci. Technol.* 54 (2020) 8473–8481.
 - [39] L. Wang, H. Xu, N. Jiang, Z. Wang, J. Jiang, T. Zhang, Trace cupric species triggered decomposition of peroxymonosulfate and degradation of organic pollutants: Cu(III) being the primary and selective intermediate oxidant, *Environ. Sci. Technol.* 54 (2020) 4686–4694.
 - [40] S. Liu, Z. Zhang, F. Huang, Y. Liu, L. Feng, J. Jiang, L. Zhang, F. Qi, C. Liu, Carbonized polyaniline activated peroxymonosulfate (PMS) for phenol degradation: role of PMS adsorption and singlet oxygen generation, *Appl. Catal. B: Environ.* (2021) 286.
 - [41] E.-T. Yun, J.H. Lee, J. Kim, H.-D. Park, J. Lee, Identifying the nonradical mechanism in the peroxymonosulfate activation process: singlet oxygenation versus mediated electron transfer, *Environ. Sci. Technol.* 52 (2018) 7032–7042.
 - [42] Y. Li, J. Yang, M. Zhang, Z. Yang, K. Shih, G.-G. Ying, Y. Feng, Coupled adsorption and surface-bound radical-mediated oxidation on biomass-derived porous carbon: a selective approach for sulfamethoxazole removal, *Chem. Eng. J.* (2023) 452.
 - [43] H. Wang, L. Gao, Y. Xie, G. Yu, Y. Wang, Clarification of the role of singlet oxygen for pollutant abatement during persulfate-based advanced oxidation processes: Co (3)O(4)@CNTs activated peroxymonosulfate as an example, *Water Res* 244 (2023) 120480.
 - [44] C. Guan, J. Jiang, S. Pang, C. Luo, J. Ma, Y. Zhou, Y. Yang, Oxidation kinetics of bromophenols by nonradical activation of peroxydisulfate in the presence of carbon nanotube and formation of brominated polymeric products, *Environ. Sci. Technol.* 51 (2017) 10718–10728.
 - [45] J. Zhu, S. Wang, H. Li, J. Qian, L. Lv, B. Pan, Degradation of phosphonates in Co (II)/peroxymonosulfate process: Performance and mechanism, *Water Res* 202 (2021) 117397.
 - [46] W. Ren, G. Nie, P. Zhou, H. Zhang, X. Duan, S. Wang, The intrinsic nature of persulfate activation and N-doping in carbocatalysis, *Environ. Sci. Technol.* 54 (2020) 6438–6447.
 - [47] T. Zhang, Y. Chen, Y. Wang, J. Le Roux, Y. Yang, J.P. Croue, Efficient peroxydisulfate activation process not relying on sulfate radical generation for water pollutant degradation, *Environ. Sci. Technol.* 48 (2014) 5868–5875.
 - [48] X. Duan, H. Sun, Z. Shao, S. Wang, Nonradical reactions in environmental remediation processes: Uncertainty and challenges, *Appl. Catal. B: Environ.* 224 (2018) 973–982.
 - [49] X. Chen, S. Qian, Y. Ma, J. Zhu, S. Shen, J. Tang, Y. Ding, S. Zhi, K. Zhang, L. Yang, Z. Zhang, Efficient degradation of sulfamethoxazole in various waters with peroxymonosulfate activated by magnetic-modified sludge biochar: surface-bound radical mechanism, *Environ. Pollut.* 319 (2023) 121010.
 - [50] W. Ren, P. Zhou, G. Nie, C. Cheng, X. Duan, H. Zhang, S. Wang, Hydroxyl radical dominated elimination of plasticizers by peroxymonosulfate on metal-free boron: kinetics and mechanisms, *Water Res* 186 (2020) 116361.
 - [51] H. Shao, J. Chen, J. Xu, Y. Liu, H. Dong, J. Qiao, X. Guan, Naproxen as a turn-on chemiluminescent probe for real-time quantification of sulfate radicals, *Environ. Sci. Technol.* 57 (2023) 8818–8827.
 - [52] L. Wu, T. Wu, Z. Liu, W. Tang, S. Xiao, B. Shao, Q. Liang, Q. He, Y. Pan, C. Zhao, Y. Liu, S. Tong, Carbon nanotube-based materials for persulfate activation to degrade organic contaminants: properties, mechanisms and modification insights, *J. Hazard Mater.* 431 (2022) 128536.
 - [53] Z. Wang, G. Chen, S. Patton, C. Ren, J. Liu, H. Liu, Degradation of nitrilotris-methylenephosphonic acid (NTMP) antiscalant via persulfate photolysis: Implications on desalination concentrate treatment, *Water Res* 159 (2019) 30–37.
 - [54] W.J. Mcelroy, S.J. Waygood, Kinetics of the Reactions of the SO₄ Radical with SO₄²⁻, S₂O₈²⁻, H₂O and Fe²⁺, Springer Netherlands, 1990.
 - [55] P. Neta, R.E. Huie, A.B. Ross, Rate constants for reactions of inorganic radicals in aqueous solution, *J. Phys. Chem. Ref. Data* 17 (1988) 1027–1284.
 - [56] Y. Gao, Z. Chen, Y. Zhu, T. Li, C. Hu, New insights into the generation of singlet oxygen in the metal-free peroxymonosulfate activation process: important role of electron-deficient carbon atoms, *Environ. Sci. Technol.* 54 (2020) 1232–1241.
 - [57] B.-T. Zhang, Z. Yan, Y. Liu, Z. Chen, Y. Zhang, M. Fan, Nanoconfinement in advanced oxidation processes, *Crit. Rev. Environ. Sci. Technol.* (2022) 1–32.
 - [58] Z.F. Cui, Y. Jiang, R.W. Field, *Fundamentals of Pressure-Driven Membrane Separation Processes*, (2010).
 - [59] N. Giovambattista, P.J. Rossy, P.G. Debenedetti, Effect of pressure on the phase behavior and structure of water confined between nanoscale hydrophobic and hydrophilic plates, *Phys. Rev. E Stat. Nonlin Soft Matter Phys.* 73 (2006) 041604.
 - [60] S. Zhang, T. Hedtke, X. Zhou, M. Elimelech, J.-H. Kim, Environmental applications of engineered materials with nanoconfinement, *ACS EST Eng.* 1 (2021) 706–724.
 - [61] M. Majumder, N. Chopra, R. Andrews, B.J. Hinds, Nanoscale hydrodynamics: enhanced flow in carbon nanotubes, *Nature* 438 (2005) 44.
 - [62] K. Gopinadhan, S. Hu, A. Esfandiari, M. Lozada-Hidalgo, F.C. Wang, Q. Yang, A. V. Tyurnina, A. Keerthi, B. Radha, A.K. Geim, Complete steric exclusion of ions and proton transport through confined monolayer water, *Science* 363 (2019) 145–148.
 - [63] Q.V. Ly, L. Cui, M.B. Asif, W. Khan, L.D. Nghiem, Y. Hwang, Z. Zhang, Membrane-based nanoconfined heterogeneous catalysis for water purification: a critical review, *Water Res* 230 (2023) 119577.
 - [64] X.A.M. Mutke, K. Tavichaiyuth, F. Drees, H.V. Lutze, T.C. Schmidt, Oxidation of the nitrogen-free phosphonate antiscalants HEDP and PBTC in reverse osmosis concentrates: Reaction kinetics and degradation rate, *Water Res* 233 (2023) 119571.
 - [65] Z.B. Xu, W.L. Wang, N. Huang, Q.Y. Wu, M.Y. Lee, H.Y. Hu, 2-Phosphonobutane-1,2,4-tricarboxylic acid (PBTCa) degradation by ozonation: kinetics, phosphorus transformation, anti-precipitation property changes and phosphorus removal, *Water Res* 148 (2019) 334–343.
 - [66] N. Huang, Z.-b Xu, W.-L. Wang, Q. Wang, Q.-Y. Wu, H.-Y. Hu, Ozonation of phosphonate antiscalant 1-hydroxyethane-1,1-diphosphonic acid in reverse osmosis concentrate: kinetics, phosphorus transformation, and anti-precipitation property changes, *Sep. Purif. Technol.* 297 (2022).
 - [67] X. Wang, H. Li, C. Shan, B. Pan, Construction of model platforms to probe the confinement effect of nanocomposite-enabled water treatment, *Chem. Eng. J. Adv.* 9 (2022).

- [68] S. Pan, X. Nie, X. Guo, H. Hu, B. Liu, Y. Zhang, Enhanced removal of phosphonates from aqueous solution using PMS/UV/hydrated zirconium oxide process, *Chin. Chem. Lett.* 34 (2023).
- [69] Y. Zhen, Z. Sun, H. Qie, Y. Zhang, C. Liu, D. Lu, W. Wang, Y. Tian, J. Ma, Selectively efficient removal of micropollutants by N-doped carbon modified catalytic ceramic membrane: synergy of membrane confinement and surface reaction, *Appl. Catal. B: Environ.* (2023) 324.
- [70] S. Pan, X. Guo, X. Lu, R. Li, H. Hu, X. Nie, B. Liu, R. Chen, M. Zhu, S. Hei, X. Zhu, S. Zhang, H. Zhou, Boosting peroxymonosulfate activation by a novel bifunctional core-shell nanoreactor MnFe₂O₄@HZO for nitrilotris-methylenephosphonic acid removal, *Appl. Catal. B: Environ.* 330 (2023).
- [71] E. Rott, R. Minke, U. Bali, H. Steinmetz, Removal of phosphonates from industrial wastewater with UV/Fe(II), Fenton and UV/Fenton treatment, *Water Res.* 122 (2017) 345–354.
- [72] L. Shao, X.Q. Cheng, Y. Liu, S. Quan, J. Ma, S.Z. Zhao, K.Y. Wang, Newly developed nanofiltration (NF) composite membranes by interfacial polymerization for safranin O and aniline blue removal, *J. Membr. Sci.* 430 (2013) 96–105.